FINAL TECHNICAL REPORT: USGS AWARD G18AP00092

A Rupture Directivity Adjustment Model Applicable to the NGA-West2 Ground Motion Models and Complex Fault Geometries

Jeff Bayless

AECOM
One California Plaza
300 S. Grand Avenue
Los Angeles, 90071, CA, USA
jeff.bayless@aecom.com
916 390 8016

Paul Somerville

AECOM
One California Plaza
300 S. Grand Avenue
Los Angeles, 90071, CA, USA
paul.somerville@aecom.com
213 996 2220

Andreas Skarlatoudis

AECOM
One California Plaza
300 S. Grand Avenue
Los Angeles, 90071, CA, USA
andreas.skarlatoudis@aecom.com
213 996 2313

Grant Period:
January 2018 through February 2020

Submitted on:
May 26, 2020

This material is based on work supported by the U.S. Geological Survey (USGS), Department of the Interior, under USGS award number (G18AP00092). The views and conclusions contained in this document are those of the authors and should not be interpreted as representing the opinions or policies of the U.S. Geological Survey. Mention of trade names or commercial products does not constitute their endorsement by the U.S. Geological Survey.

Table of Contents

1. Abstract

We present an updated directivity adjustment model, which supersedes our BS13 (Spudich et al., 2013) and SSGA (Somerville et al., 1997) models. The model retains, for the most part, the computational simplicity of both previous versions. We value the relative computational simplicity because it allows for straightforward implementation in seismic hazard analyses. Although it is relatively simple, users will notice some degree of added model complexity. This arises from the desire to model the directivity effect as a narrowband phenomenon and to accommodate complex and multi-segment ruptures.

The current model incorporates several advances over previous versions. These include the ability to handle complex rupture geometries, a zero-centered directivity effect, a narrowband formulation, the use of finite-fault simulations to guide model development, addition of an aleatory variability adjustment, and, finally, greatly improved documentation by way of this report.

To establish the narrowband formulation, we have closely followed the algorithm set forth by Spudich and Chiou (2013) to model the magnitude- and period- dependence of the directivity effect. The model also relies on the generalized coordinate system GC2, as formulated by Spudich and Chiou (2015).

The model is based on RotD50 (defined in Boore, 2010) within-event residual analyses and should be used to adjust existing RotD50-based Ground Motion Models (GMMs) which do not account for directivity effects. We evaluate three NGA-West2 GMMs: Abrahamson et al. (2014), Boore et al. (2014), and Campbell and Bozorgnia (2014) and do not discern large differences between the models developed from individual GMMs versus from the average of these GMMs. Therefore, in forward application, the model is designed to be used with these models on average or individually.

The median and standard deviation adjustment models are appropriate over the period range 0.01 to 10 seconds, in the magnitude range **M**5.0-8.0, and have a footprint which is magnitude and style-of-faulting dependent, with a maximum of 80 km distance from the fault trace. The model makes several assumptions and is not without its shortcomings; the reader is referred to Section 4.5 for a discussion of these. A MATLAB implementation of the model is provided in Appendix A.

2. Background

In their innovative paper, Somerville et al. (1997, SSGA hereafter) developed an empirical model for the modification of ground motion models (GMMs) to account for spatial variations in near-source ground motion amplitude and duration, due to the effects of rupture propagation, source radiation pattern, and the polarization of seismic waves. These effects, categorized jointly as rupture “directivity” effects, can have varying consequences on the ground motions in the near field, depending on the style of faulting and the source-site geometry. Forward directivity occurs when two conditions are met: the rupture front propagates toward the site (at a velocity close to the shear wave velocity), and the direction of slip on the fault is aligned with the site (SSGA). Forward directivity conditions are characterized by coherent pulses of the seismic energy, leading to increased ground motion amplitudes over a shortened duration relative to ordinary ground motions. An insight implicitly identified in the SSGA paper is that the forward directivity effect is stronger when the distance the rupture travels is longer (Spudich et al., 2013). Backward directivity occurs when the rupture propagates away from the site, and gives rise to longer duration motions having low amplitudes at long periods (Somerville, 2003). In addition to amplitude and duration effects, the radiation pattern of the shear dislocation on the fault causes the ground motion pulse to be oriented in the direction perpendicular (fault-normal, FN) to the fault, causing the FN ground motions to be larger than the fault-parallel (FP) motions at long periods (SSGA). Somerville (2003) empirically confirmed that the near fault rupture directivity pulse is a narrow frequency band pulse whose period increases with magnitude. This finding is theoretically consistent with the physics of a fault rupture, because source parameters such as the rise time (duration of slip at a point on the fault) and the fault dimensions generally increase with magnitude (Somerville, 2003).

Numerous examples of strong directivity effects exist in recorded ground motions, including recordings of the 1992 Landers, California earthquake, the 1999 Chi-Chi, Taiwan earthquake, the 1999 Kocaeli, Turkey earthquake, the 1994 Northridge, California earthquake, and the 1995 Kobe earthquake. In Figure 2-1, we reproduce the classical example of directivity effects captured in recordings of the 1992 Landers earthquake, as illustrated by SSGA. The aforementioned effects of forward and backward directivity can easily be seen in the velocity waveforms at the Lucerne and Joshua Tree sites, respectively.

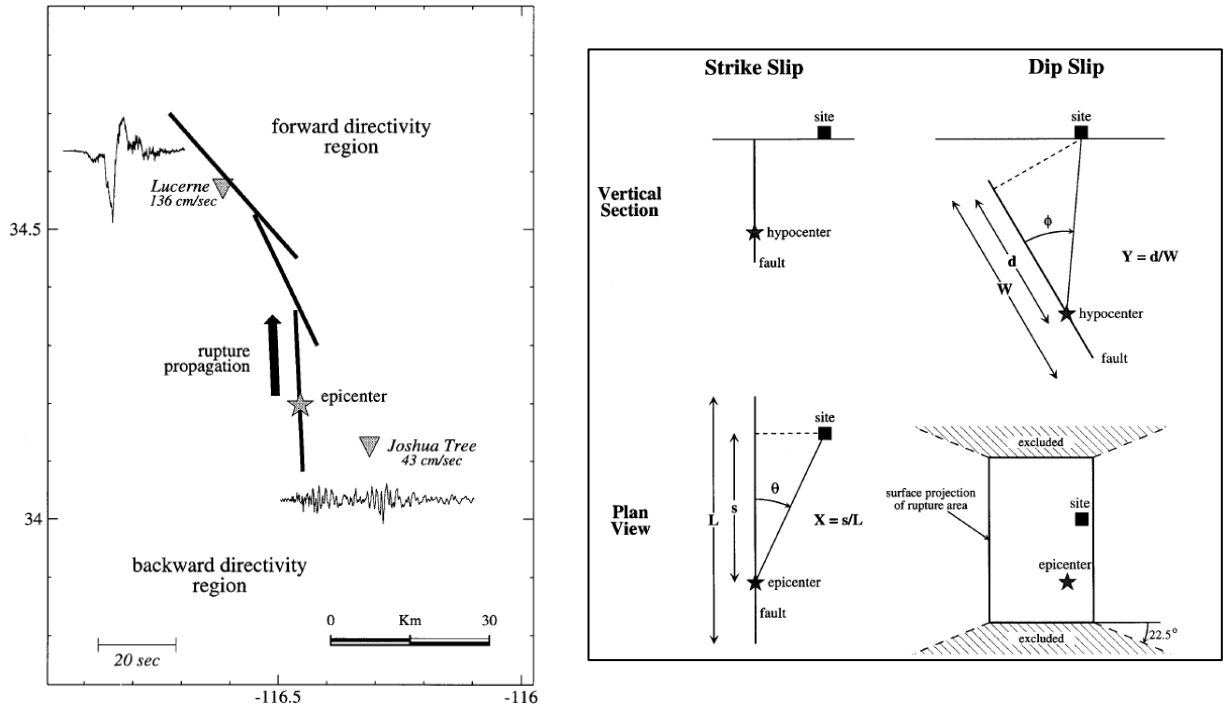

Figure 2-1. Left: Map of the 1992 Landers earthquake region, including velocity waveforms at the Lucerne (forward directivity) and Joshua Tree sites. Right: Definition of the SSGA rupture directivity parameters X, θ, Y, and ϕ. Source: SSGA.

2.1. Report Outline

Following this introductory section, Section 3 describes the general approach taken to develop the model. Section 4 provides a complete description of the directivity median adjustment model, its parameters, model coefficients, and recommendations on adjustments to the aleatory variability of GMMs. Section 5 outlines in more detail the development of the model components. In Section 6, several examples are provided for scenario earthquakes. Conclusions and recommended next steps are given in Section 7. Appendices A through D provide supplemental information.

2.2. Significance and Challenges

It is well known that ground motions under forward directivity conditions have amplified intensity, as described above, and thus can increase the seismic hazard for a site (e.g. Abrahamson, 2000; Shahi, 2013; Tarbali et al., 2016, Spagnulo et al., 2012). Methods to include directivity effects in probabilistic seismic hazard assessments (PSHAs) have been proposed in the literature (e.g., Abrahamson, 2000; Tothong et al., 2007; Shahi, 2013; Rodriguez-Marek and Cofer, 2009; Donahue et al., 2019). In the response spectral approach, which we adopt, rupture directivity effects are considered by modifications to the elastic acceleration response spectrum at 5% damping. This approach lends itself readily to inclusion into PSHA (Rodriguez-Marek and Cofer, 2009).

The effects of rupture directivity on near-fault ground motions are known to be significant and should be included to accurately estimate the hazard from long period ground motions (Abrahamson, 2000). However, these effects are not explicitly accounted for in typical GMMs, and therefore not in typical PSHAs. In our opinion, the two primary obstacles preventing typical PSHAs from including directivity effects are:

1. The added computational complexity required to include them, derived from the need to model hypocenter location.
2. Uncertainty in practice about which directivity model or models to use, how to use them, and how to calculate the required directivity parameters.

As described by Abrahamson (2000) in relation to the first obstacle, sampling the hypocenter locations from a distribution to account for rupture directivity effects adds substantial computational costs to the hazard calculation, so this is not always performed. However, for most modern hazard analysts, large computation costs are manageable. For this reason, and because we have received numerous requests from investigators and practitioners to explain the application of our 2013 model, especially for complex ruptures, we believe that the second obstacle is the primary bottleneck, and if clarified, directivity effects can more commonly be included in practice. This is the intention of this study.

Aside from implementation obstacles, there are some challenges associated with developing empirical directivity models (or, similarly, GMMs explicitly accounting for directivity effects.) One challenge is simply a shortage of recorded near-fault data, especially those that are recorded at azimuthally well-distributed stations (Spudich and Chiou, 2008). In addition, the azimuthal distribution of ground motions around recorded events is strongly correlated with the slip distribution, making it difficult to separate the effects of directivity from the effects of proximity to maximum slip (Spudich and Chiou, 2008).

There are other challenges specific to using the approach of fitting a directivity adjustment model to existing GMM residuals. First, the average directivity effect in the observed dataset is already implicitly included in the median of the GMM, and the reference directivity condition corresponding to that median motion is unclear without evaluation (Spudich et al., 2013). Second, this approach also raises the question of whether the database used in creating the GMM is biased due to sampling bias of the source-site azimuths (Spudich et al., 2013). For example, if the recorded database contains more forward directivity condition recordings than backward directivity condition recordings, then the median prediction would be biased high. A third challenge is developing a so-called “centered” directivity adjustment. Centering a predictor variable is required when a model predicts a positive directivity effect for all azimuths, which if applied to an existing GMM model, would alter the magnitude and distance scaling. For such a directivity predictor, the act of centering involves modifying the directivity adjustment so that, for a given distance from a fault, the average correction over all azimuths is zero. These issues are all addressed in this update to our model and are discussed in more detail in Section 3.

2.3. A Review of Directivity Models

In this section, we provide a brief review of past directivity models, separated into three eras: pre-NGA-West1, NGA-West1, and NGA-West2 and beyond.

Pre-NGA-West1 era

Somerville et al, (1997; SSGA) is the original directivity model. SSGA introduced two insights into the directivity effect: (1) the amplification will be greatest in some cone or wedge radiating from the hypocenter in the direction of rupture because both true directivity and the SH radiation pattern have narrow zones of amplification, and (2) the effect is stronger when the distance the rupture travels is longer (Spudich et al., 2014). SSGA empirically parameterized the effect with X and θ for strike-slip faults, and Y and ϕ for dip-slip faults, as shown in Figure 2-1. X is defined as the length of the strike-slip fault rupturing towards a site, normalized by the total rupture length. θ is the angle between the direction of rupture propagation and the direction of waves traveling from the fault to the site. Similarly, for dip-slip faults, Y is the width of the fault rupturing up-dip towards a site, normalized by the total rupture width. ϕ is the angle between the direction of up-dip rupture propagation and the direction of waves traveling from the fault to the site on the ground surface. Note that these parameters have since been redefined, as described in Section 3.

Though it was groundbreaking, the SSGA model has practical shortcomings. The normalization of the parameter X means that, for example, two different ruptures with an order of magnitude difference in length can have the same X value. Instead, this value should be un-normalized and scale with the length of the rupture directed towards a site. From the practical side, the SSGA model did not have a rupture distance dependence, has excluded zones of the directivity effect for dip-slip faults, and is a step function of magnitude. The SSGA model was updated by Abrahamson (2000) to incorporate a directivity saturation effect (at X$cos\theta = 0.4$) and to taper it at small magnitudes and large distances. Abrahamson (2000) also introduced a model for modification of the GMM aleatory variability.

A shortcoming of both the SSGA and the Abrahamson (2000) models is the “broadband” nature of them: the adjustment decreases or increases the amplitudes of the spectral ordinates monotonically with respect to increasing period (Somerville, 2003). Somerville (2003) empirically confirmed that the near-fault, fault-normal forward rupture directivity velocity pulse is a narrow band pulse whose period increases with magnitude. This finding illustrated the need to develop a “narrowband” model, in which the peak period of the directivity adjustment scales with magnitude.

The Bray and Rodriguez-Marek (2004) model proposed empirical relationships for predicting peak ground velocity, velocity pulse period, and number of significant pulses for near fault motions, including variability. Relative to modern standards, this study used a small database consisting of near-fault ground motion recordings within 20 km of shallow crustal earthquakes.

NGA-West1 era

The Next Generation of Ground-Motion Attenuation Models for the western United States (NGA-West1) program was a multidisciplinary research program coordinated by the Lifelines Program of the Pacific Earthquake Engineering Research Center (PEER, http://peer.berkeley.edu/ngawest). In this project, directivity was not included as an explicit term in the GMMs that were developed. Instead, directivity functions were developed by groups of modelers (e.g., Spudich and Chiou 2008, Rowshandel 2010) as post-hoc corrections to the median of the GMMs by fitting directivity functional forms to the residuals of that GMM (Spudich et al., 2014). This approach was subject to the challenges identified above.

Spudich and Chiou (2008) developed physically-based predictor variables using isochrone theory (isochrone directivity predictor, IDP). Spudich and Chiou (2008) used finite fault simulations to explore the predictor variable space before creating broadband empirical models from the NGA-West1 residuals.

Rowshandel (2006) developed an intuitive model grounded in the two SSGA insights. This model generalized the SSGA model by removing the need to classify faults by style of faulting and by performing an integral over the entire rupture surface. Rowshandel (2010) applied the Rowshandel (2006) directivity model to the NGA-West1 GMM residuals. This method is broadband and normalizes the directivity parameter by fault area.

NGA-West2 era and beyond

The NGA-West2 program (NGA-W2) was a follow-up to the NGA-West1 program. Task 1 of the program was to “examine the near-fault directivity effects and add these effects to the NGA models” (http://peer.berkeley.edu/ngawest2/tasks). The working group on directivity included five different teams: Bayless and Somerville (2013; BS13); Chiou and Spudich (2013; CS13); Rowshandel (2013; R13); Shahi and Baker (2013; SB13); and Spudich and Chiou (2013; SC13). These teams each created an improved directivity model using the expanded NGA-West2 dataset and incorporating conceptual and practical model advances, including the un-normalization of the predictor variables. The efforts of the directivity working group are summarized in a PEER report (Spudich et al., 2013) and the models are compared thoroughly in Spudich et al., (2014). In the Spudich et al., (2014) comparison, it is shown that the strike-slip rupture geometries are modeled similarly between the models (e.g. Figure 2-2), but for reverse faults the predicted directivity adjustments are considerably different between models (e.g. Figure 2-2), and the differences are sensitive to the assumptions of each model (Spudich et al., 2014). These inconsistencies between models have contributed to some uncertainty in practice as to which models, if any, should be used in seismic hazard assessments.

Besides the improvements in model formulation and available data, the NGA-West2 project aimed to improve over the NGA-West1 approach by incorporating some of the directivity models into the NGA-West2 GMMs, rather than developing them as corrections. Two techniques were considered for achieving this. The first was to include

the directivity functional forms in the GMM mixed-effects regression. The only NGA-West2 GMM to use this technique was Chiou and Youngs (2014). The second technique was to develop the models as corrections from GMM residuals, but to "center" them, as discussed above, to avoid modifying the magnitude and distance scaling of the GMM.

Most of the NGA-W2 directivity models have not been significantly changed since 2014. An exception is the 2018 update to Rowshandel (2014), which made improvements on narrow-band characterization, centering, and capturing rupture and slip heterogeneity effects (Rowshandel, 2018). At the time of writing this report, Brian Chiou (personal communication) is also using SC13 to develop directivity correction terms for the NGA-W2 GMMs.

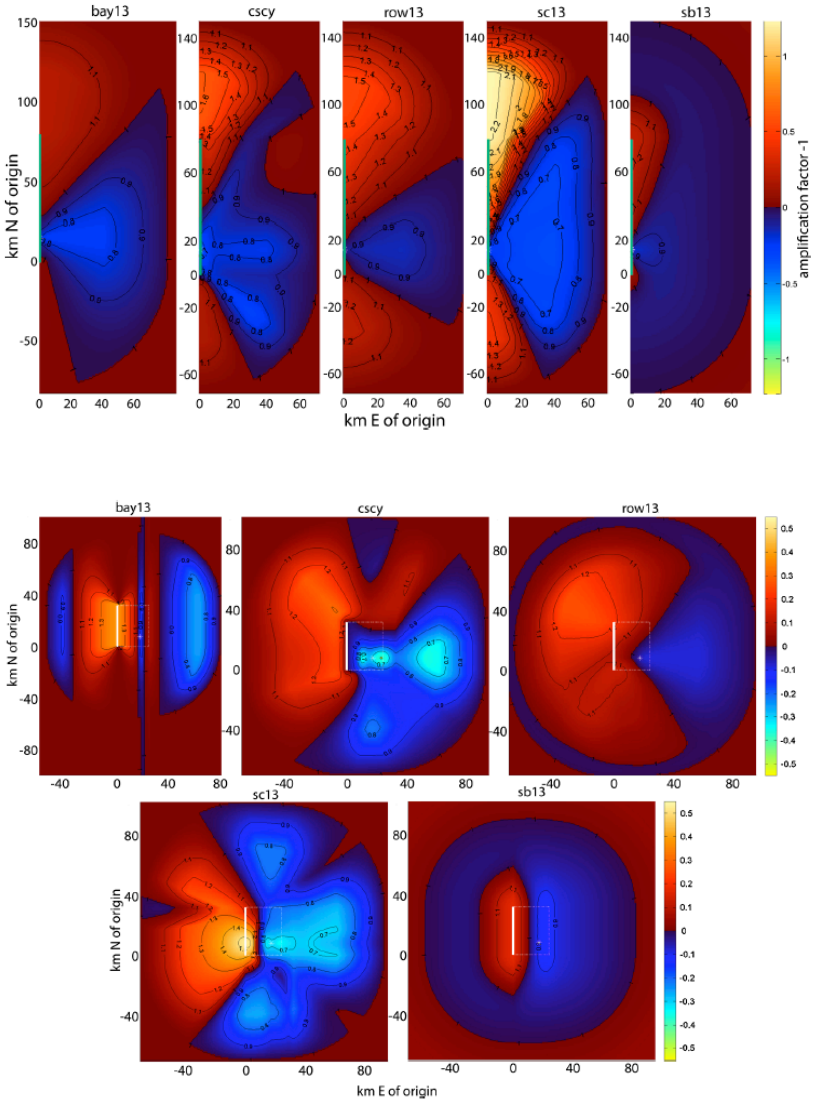

Figure 2-2. Top: Spudich et al., (2013) comparison of rupture directivity amplification factors for the five NGA-West2 models, for a **M**7.2 strike slip fault, at T=5 s period. Source: Spudich et al., (2013) Bottom: The same comparison for a **M**7.0 reverse fault, at T=5 s period. The leftmost model in each set, bay13, is the Bayless & Somerville (2013) model. Source: Spudich et al., (2013).

2.4. Needs in Practice

For practical applications, hazard analysts need a directivity model that is compatible with modern PSHA methods. For one, this means a directivity model must either be built into a GMM, be complementary to a GMM or suite of GMMs, or be compatible with generic ones. Additionally, the model must be extendable to complex fault rupture geometries, including changes along strike in strike, rake, dip, and depth, for example like the ruptures in the Uniform California Earthquake Rupture Forecast version 3 (UCERF3; Field et al., 2013) such as the Landers event (Figure 2-1). A proper directivity model should have a median prediction adjustment, along with an adjustment for the GMM standard deviation. It is advantageous, although not required, that the directivity model be straightforward enough to be understood and implemented by a well-informed user. Finally, a directivity model should provide the appropriate documentation needed to educate users on model application. We address all of these needs in this report.

PEER assembled an End-Users Directivity Panel to evaluate the status of NGA-West2 directivity models and to develop recommendations for future research on near-fault effects (Donahue et al., 2019). Directivity modelers were intentionally not part of the panel to avoid conflicts of interest, but the modelers were continuously contacted to make sure the panel understood the models. This panel performed checks on reference directivity condition in the NGA-W2 database, and concluded that the Abrahamson et al. (2014), Boore et al. (2014), and Campbell and Bozorgnia (2014) GMMs can be considered to reflect a directivity-neutral condition (Stewart et al., 2016). Donahue et al. (2019) summarized and compared the existing models, provided recommendations for which models to use in practice, and presented several methods for including these methods (median adjustment) in seismic hazard analyses. The most complete hazard implementation method (their Option 5) is hypocenter randomization, which adds an additional integral to the hazard calculation. This panel stopped short of making recommendations for adjustments to the aleatory variability of GMMs, because this effect is poorly developed in the literature (Donahue et al, 2019); this need is addressed in this report.

3. Approach Overview

In this report, we present a ground-motion directivity adjustment model (hereafter "the model") which is an update of a previous version, BS13, which itself was an improvement of the classic model SSGA. The current model supersedes both previous versions. Our model retains, for the most part, the computational simplicity of both previous versions. We value the relative computational simplicity because it allows for straightforward implementation into seismic hazard analyses.

The model is rooted in two basic SSGA insights, namely that (1) forward directivity occurs when the rupture front propagates toward the site (at a velocity close to the shear wave velocity), and the direction of slip on the fault is aligned with the site. (2) The directivity effect is stronger when the distance the rupture travels is longer. Together, these two insights imply that that the directivity amplification will be largest in areas where simultaneously the SH radiation pattern lobe (for a point-source double couple at the hypocenter) is peaked and in areas where the rupture has propagated in that direction for some distance.

The model is based on a ground-motion residual analysis using the RotD50 horizontal component of 5% damped spectral acceleration. Therefore, it is this intensity measure (IM) for which the model predicts directivity adjustments to the median and aleatory variability. In BS13, we developed separate models for the FN and FP horizontal components. Most seismic hazard analyses are currently performed using RotD50, including the national seismic hazard maps (Peterson et al., 2014), therefore it was the IM of focus for this study. We anticipate updating the model with FN and FP components in the future.

In the model development (and application) restrictions are imposed on the geometry of earthquake ruptures, as in Spudich et al. (2013). All fault *segments* are assumed to be rectangular planes with horizontal tops and bottoms, and with a discrete strike angle and dip angle. One or more fault segments compose contiguous fault *strands* (which may model changes in strike and dip), and one or more fault segments compose a complete *rupture*. Multi-fault ruptures consist of multiple fault strands and may be discontinuous. We follow the Aki and Richards (1980) convention where segments always dip to the right when looking along the strike direction, strike angles are measured clockwise from north, and dip angles are less than or equal to 90 degrees.

A model attribute which has been discussed by others (e.g. Donahue et al., 2019) is that of "centering". Centering refers to the process of modifying a directivity adjustment model such that is has on average a null change in the ground motion prediction. This requirement was brought forward by Norm Abrahamson in the NGA-West2 phase of directivity models, when it was discovered that some models predicted a positive (amplification) effect for all azimuths at a given distance. Applying such a model to an existing GMM would effectively modify the magnitude and distance scaling built into that GMM, therefore centering was a requirement before these models could be used. However, a model like ours that is built upon GMM residuals (which are assumed to have on average a centered directivity effect, this has been confirmed by Donahue et al., 2019)

does not need to go through the centering process. The residuals themselves center the model, because it predicts both forward and backward directivity effects.

The model is established in five stages and an overview of these stages is provided here. The process and results for each stage are outlined in detail in Section 5.

3.1. Stage 1: Simulations

We use a rich database of simulations, as described in Section 5.1, to explore the directivity predictor variable space. For each set of simulations, we create a database of 5% damped RotD50, ranging from 10s spectral period down to the lowest usable period of the simulations. We calculate ground-motion residuals from three NGA-West2 GMMs: Abrahamson et al. (2014; ASK14), Boore et al. (2014; BSSA14), and Campbell and Bozorgnia (2014; CB14). The Chiou and Youngs (2014; CY14) model was excluded because this model already implements directivity effects. The residuals at a given spectral period are mapped to evaluate the spatial trends and plotted versus the directivity parameters we consider candidates to use in the model, based on the SSGA principles of forward directivity described previously. Examples of the Stage 1 analyses are given in Figure 3-1 and Figure 3-2.

Using these residuals, we explore the directivity predictor variable space to develop the ad-hoc directivity predictor (defined as a combination of multiple directivity parameters) and the functional form for our directivity adjustment model. We ensure that this parameterization is flexible enough to accommodate complex fault geometries and multi-segment ruptures.

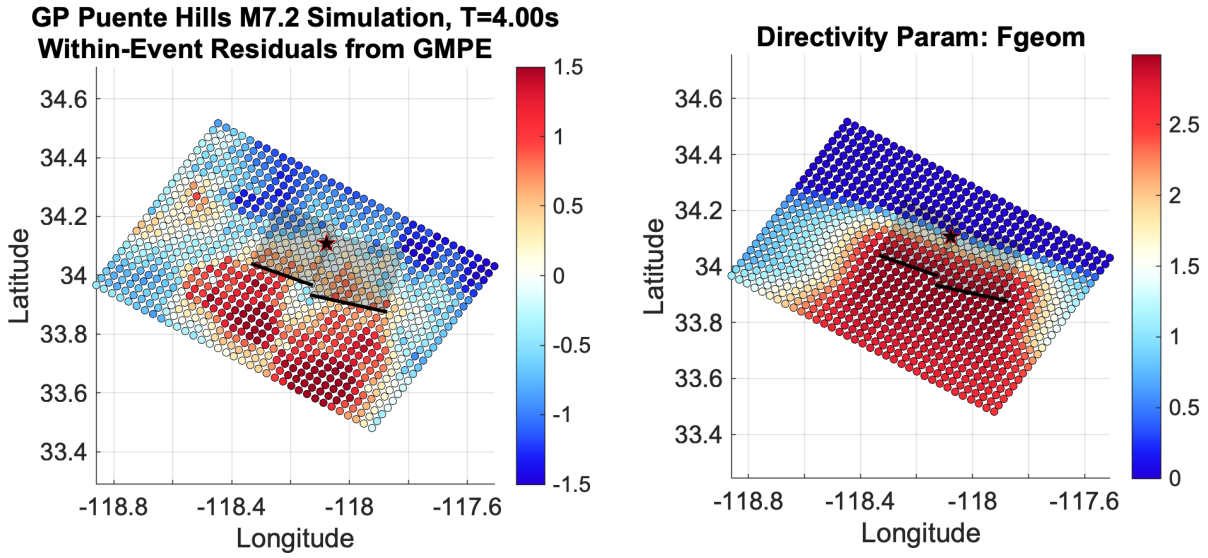

Figure 3-1. Maps of the dense grid of simulation stations (circles) of the Graves and Pitarka (2010) Puente Hills blind thrust simulations. The surface trace of the two-segment rupture is given by the heavy black line and the surface projection of the fault (dipping shallowly to the northeast) is given by the transparent black fill. The red star shows the hypocenter location. Left: NGA-West 2 GMM within-event residuals at T=4 sec. Right: Spatial variation of a candidate directivity parameter.

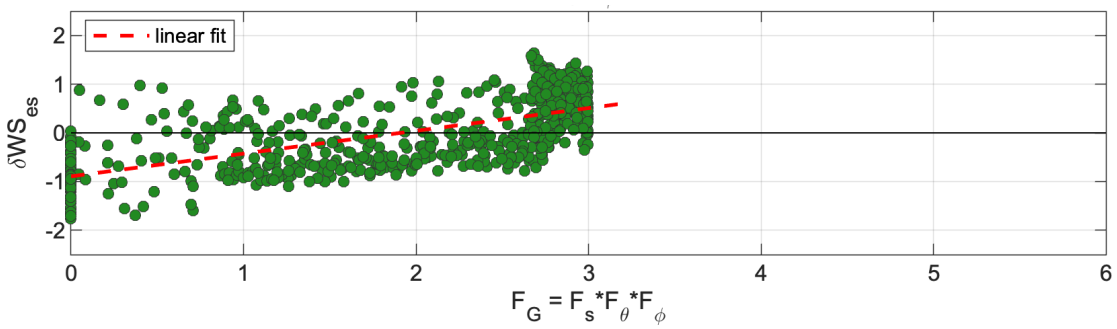

Figure 3-2. Within-event residuals (δWS_{es}) from the Graves and Pitarka (2010) Puente Hills blind thrust simulations at T=4 sec, plotted versus a candidate directivity parameter (described in Section 4), and the observed linear trend.

3.2. Stage 2: NGA-W2 Data

Using the predictor variables from Stage 1, we evaluate the residuals from the NGA-West2 database, using the same three GMMs. Tables of within-event residuals for all three GMMs have been graciously provided by the respective authors. Spudich and Chiou (2013) identified 36 earthquakes in the NGA-West2 database with a finite fault model and at least 5 recordings, and 21 of them exhibit good azimuthal coverage. We use recorded data from the same events, plus a few additional events (see Section 5.2), to evaluate trends in the residuals versus the predictor variables developed in Stage 1. An example of this process using the 1999 Chi-Chi, Taiwan earthquake data is shown in Figure 3-3.

3.3. Stage 3: Iteration and Composite Results

We iterate between Stages 1 and 2 to reconcile inconsistencies between the Stage 1 model and the directivity observed in the data. We repeat until an acceptable level of consistency (determined subjectively) is achieved between the GMM residual trends in the data and simulations, to arrive at the final model form. The combined database (simulations and data) is used to develop an ad-hoc composite model, which serves as a comparison for the regression-based model in Stage 4.

In the first three stages, the narrowband formulation is established. We closely follow the algorithm set forth by Spudich and Chiou (2013) to model the magnitude- and period-dependence of the directivity effect. The effect is quantified through the slope of the linear trend in the residuals versus the directivity predictor. A larger slope implies a stronger effect in forward and backward directivity regions. We develop relationships for the peak slope, period of the peak slope, and the directivity predictor x-intercept (the value of the directivity predictor for which the directivity effect is zero on average) as a function of magnitude. We model the bandwidth of the peak period by fitting the period-dependence of the slope parameter to a Gaussian function (to determine the Gaussian standard deviation, or width). This procedure is outlined in more detail in Section 5.

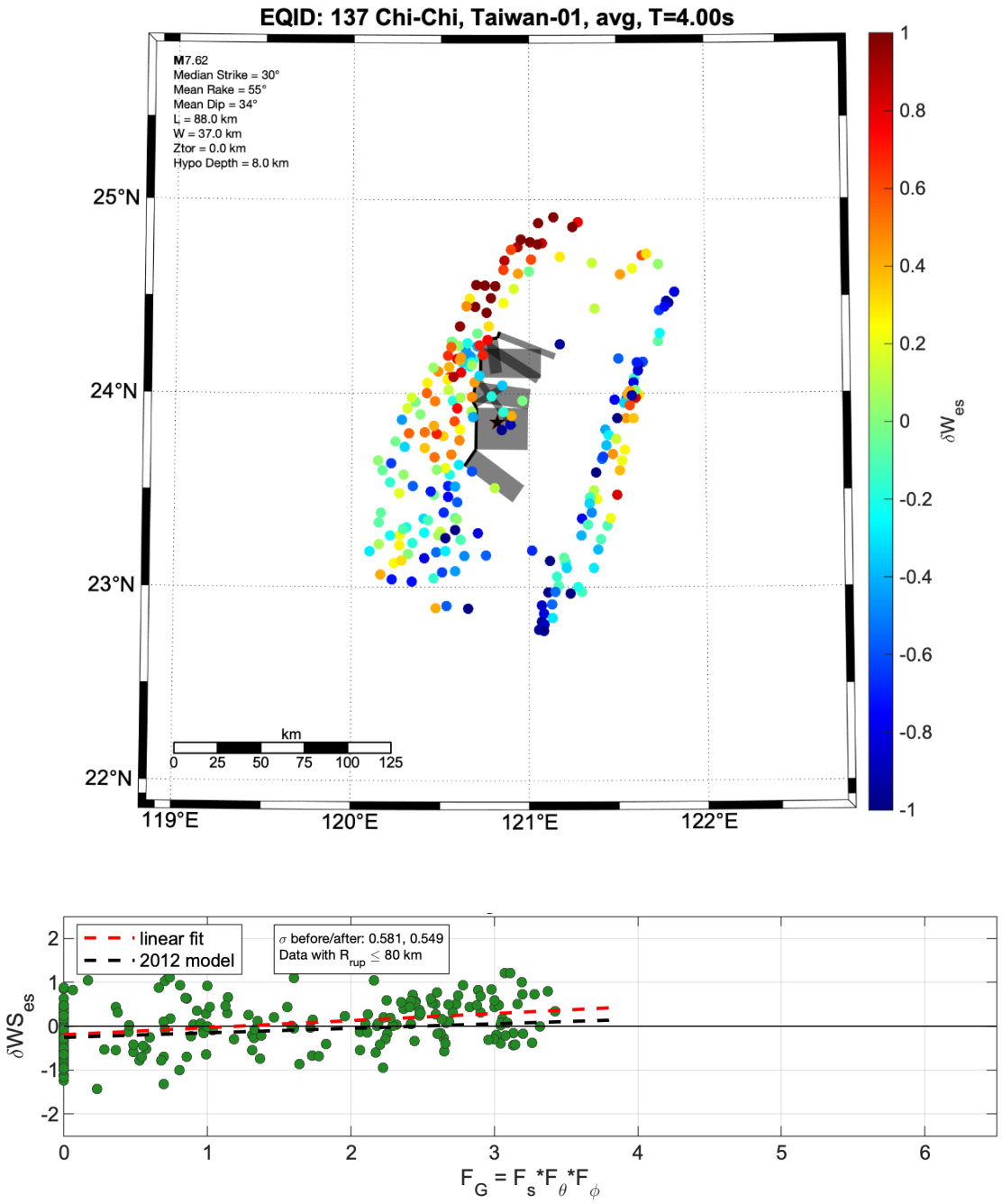

Figure 3-3. Top: A map of within-event residuals from the 1999 Chi-Chi, Taiwan earthquake, at T=4 sec. The surface trace of the rupture is given by the heavy black line and the surface projection of the fault segments (dipping primarily to the east) are given by the transparent black fill. Bottom: Within-event residuals plotted versus a candidate directivity parameter (described in Section 4), at T=4 sec.

3.4. Stage 4: Regression

A nonlinear least squares regression is performed using the combined database (simulations and data) to derive the final model coefficients. These coefficients compare favorably with the Stage 3 results.

3.5. Stage 5: Aleatory Variability

To use the directivity model in seismic hazard applications requires not only a median adjustment model, but also a model for the adjustment of the GMM aleatory variability. Adjustments to the standard deviations of three GMMs (Abrahamson et al., 2014; Boore et al., 2014; and Campbell and Bozorgnia, 2014) are estimated and an average GMM variability adjustment model is developed. To arrive at the variability model, the within-event residuals from Stage 2 (NGA-W2 data) are adjusted for median directivity effects, and the reduction in their standard deviation is calculated.

We note that the standard deviation of most GMMs is averaged over all distances, although the standard deviations of near-source residuals are often smaller than those at large distances (Abrahamson, 2000). In Figure 3-4 we show the standard deviation of within-event residuals calculated directly from the ASK14, BSSA14, and CB14 models. In this figure, the solid lines show the standard deviation calculated from all distances, and the dashed lines show the same for the subset of data with Rrup<40 km. At periods below about 4 sec, the standard deviation of the small distance data is reduced, although at periods longer than 4 sec it is increased. Most GMM creators, including those from NGA-W2, do not model any distance dependence of the standard deviation. However, this characteristic of the residuals supports our model, which reduces the GMM standard deviation for sites located within the footprint of our median adjustment model.

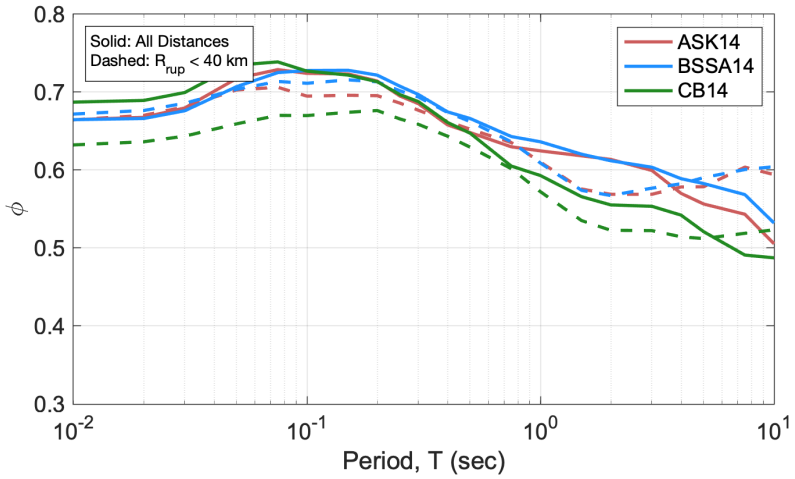

Figure 3-4. The standard deviation of within-event residuals (φ) for three NGA-W2 GMMs.

4. Model Functional Form

4.1. Coordinate System

The model relies on the generalized coordinate system GC2, as formulated by Spudich and Chiou (2015). GC2 defines the strike-normal (T) and strike-parallel (U) coordinates (in km) of sites located around complex fault geometries, including those which are neither straight nor continuous. GC2 is based on averaging the distance coordinates over the different fault segments, weighted by the inverse of the square of the distance to the surface trace. This scheme results in smoothly varying coordinates in space which are progressively dominated by the nearest segment. For a straight fault, the GC2 coordinate is a rotation of the y-axis to the fault strike direction, and the T coordinate is equivalent to the NGA-West2 distance parameter Rx. Like Rx, T is positive on the hanging wall side of a rupture and negative on the footwall side. U is positive in the direction of strike and negative in the anti-strike direction.

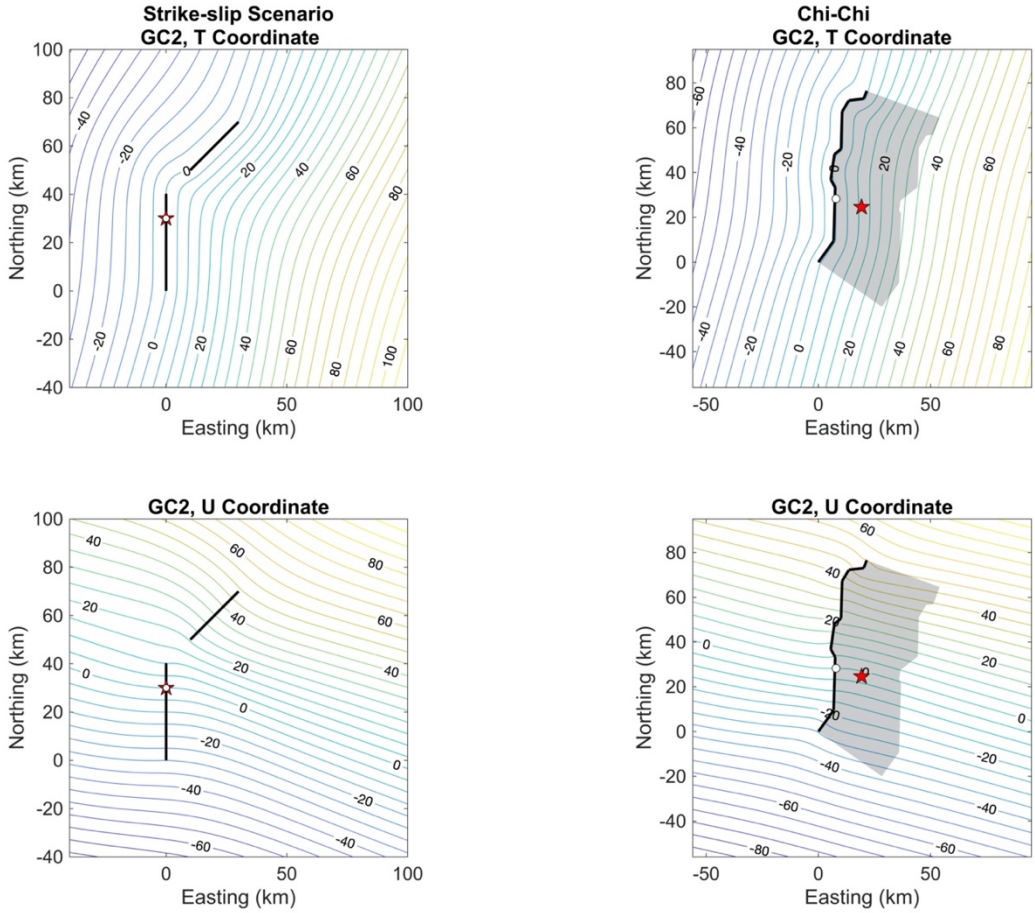

Figure 4-1. Contour maps of GC2 coordinates (T, top; U, bottom) for (left) a scenario vertical fault with two disjointed strands with distinct strike angles, and (right) the 1999 Chi-Chi, Taiwan rupture model used in NGA-West2. In both examples the hypocenter location is given by the red star, and the coordinate system origin is given by the white circle.

A very elegant, and appealing, aspect of GC2 is that the weighting integral can be solved in closed form rather than by brute force; this is computationally very efficient. Examples of the GC2 coordinate system for two earthquakes are given in Figure 4-1. Additional examples can be found in Spudich and Chiou (2015).

Spudich and Chiou (2015) prefer placing the GC2 origin at the first endpoint of the fault trace, so that U along the rupture trace is positive. For our application, we choose the origin to be the projection of the hypocenter up-dip to the ground surface. This is convenient for converting U into our directivity prediction parameter S, which is the rupture travel length measured along-strike relative to the hypocenter (described below). With this choice of origin, S is positive in the direction of strike and negative in the anti-strike direction. A MATLAB function for calculating GC2 is provided in Appendix A.

We note that the fault parallel ordinate, T (km), should not be confused with the spectral acceleration oscillator period, also denoted T (seconds). In this report, we italicize the GC2 ordinate T and provide the units of the oscillator period T (e.g. T=4 sec) whenever possible to avoid confusion.

4.2. Median Adjustment Model

Table 4-1 lists the model functions, model parameters (values used by the functions), arguments (values passed into the functions to calculate the parameters), and coefficients with a description of each.

Table 4-1. Description of model functions, parameters, arguments, and coefficients.

	Name	Description
Functions	f_D	Directivity adjustment (ln units).
	f_G	Period independent geometric directivity predictor.
	f_{S2}	Predictor function for the distance the rupture has traveled towards a site.
	f_θ	Azimuthal predictor function #1.
	f_ϕ	Azimuthal predictor function #2.
	f_{dist}	Distance taper function.
	φ_{Red}	Within-event standard deviation reduction.
Parameters	a, b	Magnitude- and period-dependent intercept and slope of the directivity adjustment.
	S	The horizontal length of the rupture travel between the site and the origin (km).
	D	The effective rupture travel width, measured from the hypocenter to the shallowest depth of the rupture plane, up-dip (km).
	$S2$	Generalized rupture travel distance parameter which accounts for S, D, and the rupture characteristic rake angle (km).
	θ	The angle made between the average fault strike direction and the vector from the origin to the site (calculated in plan view). Formulation varies by style of faulting.
	ϕ	The angle made between the vector from the bottom of the rupture plane up-dip to the ground surface, and the vector from the bottom of the rupture plane to the Rx of the site (calculated in fault cross-section-view). Formulation varies by style of faulting.
	T_{peak}	The peak period of the directivity effect (sec).
	b_{max}	The maximum slope of the directivity effect.
	f_{G0}	The magnitude-dependent directivity predictor x-intercept (the value of the directivity predictor for which the directivity effect is zero on average).
	$R_{taper}, R_{max}, R_{SOF}$	Distance parameters used in the distance taper function (km).
	R_{y0}	The horizontal distance to a site off the end of the rupture measured parallel to strike (km).
Arguments	U, T	The GC2 strike-parallel and strike-normal coordinates relative to the origin, which is defined as the projection of the hypocenter up-dip to the ground surface (km).
	SOF	The rupture style of faulting flag to distinguish between predominantly strike-slip ruptures, and all other types.
	Rupture Information	The basic information about the rupture: **M**, segment coordinates, segment lengths, segment strike angles, depth to top of rupture, rupture characteristic down-dip width, characteristic rake angle, characteristic dip angle, primary hypocenter location.
	T	The oscillator spectral period in sec (note the spectral period T is not italicized and care should be taken not to confuse T with the GC2 strike-normal coordinate, T).
Coefficients	b_1, b_2	Intercept and slope of the magnitude-dependent b_{max} relationship.
	c_1, c_2	Intercept and slope of the magnitude-dependent $\log_{10} T_{peak}$ relationship.
	d_1, d_2	Intercept and slope of the Magnitude-dependent f_{G0} relationship.
	e_1	Aleatory variability model coefficient.
	σ_g	The standard deviation (width parameter) of the Gaussian function used to model the narrowband formulation.

The median directivity adjustment in natural log units, f_D, is given by Equation 1:

$$f_D(\boldsymbol{M},\mathrm{T},x,SOF) = \left(a(\boldsymbol{M},\mathrm{T}) + b(\boldsymbol{M},\mathrm{T}) f_G(x,SOF) \right) f_{dist}(\boldsymbol{M},SOF) \quad (1)$$

where $\boldsymbol{M}$ is moment magnitude, T is the oscillator period, x is the vector of parameters describing the position of the site relative to the rupture, SOF is the style of faulting, a and b are magnitude- and period-dependent model parameters, f_{dist} is the magnitude- and SOF-dependent distance taper, and f_G is the geometric directivity predictor.

The terms of Equation 1 are given by Equations 2a-d:

$$f_G(x,SOF) = f_{S2}(x) f_\theta(x,SOF) f_\phi(x,SOF) \quad (2a)$$

$$b(\boldsymbol{M},\mathrm{T}) = b_{max}(\boldsymbol{M}) \exp\left(\frac{(\log_{10} \frac{\mathrm{T}}{\mathrm{T}_{peak}(\boldsymbol{M})})^2}{-2{\sigma_g}^2} \right) \quad (2b)$$

$$a(\boldsymbol{M},\mathrm{T}) = -b(\boldsymbol{M},\mathrm{T})\, f_{G0}(\boldsymbol{M}) \quad (2c)$$

$$f_{dist}(\boldsymbol{M},SOF) = \begin{cases} 1 - \exp\left(\dfrac{-4R_{max}(\boldsymbol{M},SOF)}{R_{taper}} + 4 \right) & For\ R_{taper} \le R_{max}(\boldsymbol{M}) \\ 0 & For\ R_{taper} > R_{max}(\boldsymbol{M}) \end{cases} \quad (2d)$$

where

$$b_{max}(\boldsymbol{M}) = b_1 + b_2 \boldsymbol{M} \quad (3a)$$

$$\log_{10} T_{peak}(\boldsymbol{M}) = c_1 + c_2 \boldsymbol{M} \quad (3b)$$

$$f_{G0}(\boldsymbol{M}) = d_1 + d_2 \boldsymbol{M} \quad (3c)$$

$$R_{taper} = \sqrt{T^2 + R_{y0}^2} \quad (3d)$$

$$R_{max}(\boldsymbol{M},SOF) = \begin{cases} 20\boldsymbol{M} - 60 - R_{SOF} & For\ 5 \le \boldsymbol{M} < 7 \\ 80 - R_{SOF} & For\ \boldsymbol{M} \ge 7 \end{cases} \quad (3e)$$

$$R_{SOF} = \begin{cases} 0 & For\ SOF = 1 \\ 20 & For\ SOF = 2 \end{cases} \quad (3f)$$

The geometric directivity predictor, f_G, and its components, are period independent. These functions only depend on the source-site geometry and the style of faulting. For notational brevity, Equations 4 through 6 suppress the dependencies x and SOF.

The rupture travel distance term f_{S2} is given by:

$$f_{S2} = \ln(S_2) \quad (4a)$$

$$S_2 = \begin{cases} D & For\ SOF = 2\ and\ S\cos(Rake) < 0 \\ \sqrt{D^2 + (S\cos(Rake))^2} & Otherwise \end{cases} \quad (4b)$$

Equation 4b is split into two cases, dependent on the style of faulting flag and the sign of the quantity $S\cos(Rake)$. The first case is specific tor normal, reverse, and oblique ruptures, for locations with negative values of this quantity, which represents all sites in the direction opposite of the unit vector from the hypocenter in the direction of the characteristic rake angle. For such locations, the parameter S_2 is set to D. For all other cases (and for all values of $S\cos(Rake)$ for ruptures classified as strike-slip) the parameter S_2 is the square root sum of squares of the effective rupture travel width and the effective rupture travel length.

Equations 4a and 4b require the parameter S, which is readily obtained from the GC2 ordinate U. Because we choose the GC2 origin to be the projection of the hypocenter up-dip to the ground surface, S is equal to U for sites within the along-strike extent of the rupture (for simple ruptures, the along-strike extent is the rupture length). For sites outside this region (i.e. for sites with nonzero R_{y0}), S is equal to the U ordinate of the nearest rupture trace endpoint. Examples of this conversion are given in Section 6.1 (e.g. Figure 6-2).

The model considers two categories of rupture types: predominantly strike-slip ruptures ($SOF = 1$) and all other categories of ruptures (reverse, normal, and oblique; $SOF = 2$). The model functions and parameters for the azimuthal predictors are given by equations 5 and 6:

$$\theta = \begin{cases} \left|\tan^{-1}\dfrac{T}{U}\right|; if\ T = U = 0;\ \theta = 0 & For\ SOF = 1 \\ \tan^{-1}\left|\dfrac{\max[\ |T|, 10(|\cos(\mathrm{Rake})| + 1)\ ]}{R_{y0}}\right| & For\ SOF = 2 \end{cases} \quad (5a)$$

$$f_\theta = \begin{cases} |\cos(2\theta)| & For\ SOF = 1 \\ \sin(\theta) & For\ SOF = 2 \end{cases} \quad (5b)$$

$$\phi = \begin{cases} 0 & For\ SOF = 1 \\ Dip - 90 + \tan^{-1}\dfrac{|T| + T_{bot}}{D_{bot}} & For\ SOF = 2\ and\ T < 0\ (footwall) \\ 90 - Dip - \tan^{-1}(\dfrac{T_{bot} - T}{D_{bot}}) & For\ SOF = 2\ and\ 0 \le T \le T_{bot}\ (hanging\ wall) \\ 90 - Dip + \tan^{-1}(\dfrac{T - T_{bot}}{D_{bot}}) & For\ SOF = 2\ and\ T > T_{bot}\ (hanging\ wall) \end{cases} \quad (6a)$$

$$f_\theta = \cos(2\phi) \quad (6b)$$

where T_{bot} is the T ordinate of the bottom of the rupture plane and D_{bot} is the vertical depth of the bottom of the rupture plane from the ground surface. The angles in Equation 6a for $SOF = 2$ are interpreted graphically in Appendix B.

The model coefficients are listed in Table 4-2.

Table 4-2. Model coefficients. The aleatory variability model coefficients are given in Table 4-4.

Coefficient	Estimated Value	Standard Error	95% Confidence Interval		Description
$\boldsymbol{b_1}$	0.5469	0.0130	0.5215	0.5724	Constant of the Magnitude-dependent b_{max} relationship
$\boldsymbol{b_2}$	-0.0336	0.0019	-0.0373	-0.0299	Slope of the Magnitude-dependent b_{max} relationship
$\boldsymbol{c_1}$	-1.2090	0.0037	-1.2162	-1.2017	Constant of the Magnitude-dependent $\log_{10}$ T$_{peak}$ relationship
$\boldsymbol{c_2}$	0.2858	0.0005	0.2847	0.2869	Slope of the Magnitude-dependent $\log_{10}$ T$_{peak}$ relationship
$\boldsymbol{d_1}$ $\boldsymbol{SOF = 1}$	-4.8300	0.0438	-4.9159	-4.7441	Constant of the Magnitude-dependent f_{G0} relationship, for $SOF = 1$
$\boldsymbol{d_2}$ $\boldsymbol{SOF = 1}$	0.9928	0.0067	0.9796	1.0060	Slope of the Magnitude-dependent f_{G0} relationship, for $SOF = 1$
$\boldsymbol{d_1}$ $\boldsymbol{SOF = 2}$	-1.5415	0.0352	-1.6104	-1.4726	Constant of the Magnitude-dependent f_{G0} relationship, for $SOF = 2$
$\boldsymbol{d_2}$ $\boldsymbol{SOF = 2}$	0.3946	0.0057	0.3835	0.4057	Slope of the Magnitude-dependent f_{G0} relationship, for $SOF = 2$
$\boldsymbol{\sigma_g}$	0.4653	0.0034	0.4586	0.4720	The standard deviation (width parameter) of the Gaussian function

4.3. Use with GMMs

The model can be used to adjust the median prediction of a non-directive GMM using Equation 7:

$$\ln\big(\, RotD50_{dir}(\boldsymbol{M},\mathrm{T},x)\big) = \ln\big(\, RotD50(\boldsymbol{M},\mathrm{T},x)\big) + f_D(\boldsymbol{M},\mathrm{T},x,SOF) \qquad (7)$$

where $RotD50_{dir}$ is the GMM prediction with the directivity adjustment, $RotD50$ is the unmodified GMM-predicted ground motion and f_D is the median directivity adjustment. The adjustment for the aleatory variability is described in Section 4.4.

The model is developed using residuals calculated from the average of three NGA-West2 GMMs: Abrahamson et al. (2014), Boore et al. (2014), and Campbell and Bozorgnia (2014). In general, we did not observe large differences between the model developed from residuals using the average of these GMMs versus the models developed from individual GMM residuals. Therefore, in forward application, it is designed to be used with these models on average or individually. We also deem it applicable to any modern GMM for RotD50 from crustal earthquakes that does not already account for rupture directivity.

To use the model requires:

1. Definition of the earthquake rupture, which includes **M,** segment coordinates, segment lengths, segment strike angles, the depth to the top of rupture, the rupture characteristic down-dip width, the rupture characteristic rake angle, the rupture characteristic dip angle, the characteristic style of faulting, and a primary hypocenter location.
2. The position of the site relative to the rupture, U and T, derived from the earthquake description and the site coordinates.
3. The spectral period of interest, T.

Examples of these requirements for a set of earthquake scenarios are given in Section 6.1. Appendix A includes a suite of MATLAB scripts for these calculations. Table 4-3 lists a few special constraints we impose on the directivity parameters.

Table 4-3. Imposed constraints on select parameters.

Function or Parameter	Constraint	Comment
$\boldsymbol{D}$	$D \geq 3$	Minimum value of 3 km so that $\ln(S2)$ is positive in all cases.
$\boldsymbol{f_{S2}}$	For SOF=1, $f_{S2} \leq \ln(465)$	Capped at ln(465) km, or approximately the rupture length of a strike-slip $\boldsymbol{M}8$
	For SOF=2, $f_{S2} \leq \ln(188)$	Capped at ln(188) km, or approximately the diagonal dimension of a reverse $\boldsymbol{M}8$
$\boldsymbol{M}$	$5.0 \leq \boldsymbol{M} \leq 8.0$	The scaling relations for the model were developed using the range $5.5 \leq \boldsymbol{M} \leq 7.9$, see discussion below.

The model is appropriate over the period range 0.01 to 10 seconds, for distances up to 80 km from the rupture surface trace (and is technically applicable for all distances, because beyond 80 km distance the effect is zero, see Section 4.5). The model is developed using earthquakes in the range **M**5.5-7.9, therefore it is appropriate to use in this range. We have tested the model for scenario earthquakes ranging from **M**5.0 to **M**8.0 (Section 6) and are satisfied with the model behavior, therefore we deem it acceptable in the range **M**5.0-8.0. For magnitudes below 5.5, we recommend using the scaling relations for a **M**5.5 earthquake (e.g. allow the fault dimensions to scale appropriately but use the relationships in Equations 2 and 3 with **M**=5.5.) This feature is built into the MATLAB functions provided in Appendix A.

4.4. Standard Deviation Adjustment Model

The GMM between-event and within-event residuals are well-represented as zero-mean, independent, normally distributed random variables with standard deviations τ and φ (Al Atik et al., 2010). The total standard deviation in natural log units, σ, is given by Equation 8.

$$\sigma = \sqrt{\tau^2 + \varphi^2} \tag{8}$$

If φ_{NoDir} is the within-event standard deviation from an existing GMM without accounting for directivity, then the within-event standard deviation for use with the GMM when including the directivity adjustment, φ_{Dir}, is calculated using Equation 9.

$$\varphi_{Dir}^2 = \varphi_{NoDir}^2 - \varphi_{Red}^2 \tag{9a}$$

$$\varphi_{Red}(\mathrm{T}, R_{rup}, \boldsymbol{M}, SOF) = \begin{cases} e_1(\mathrm{T}) & For\ R_{rup} < R_{max}(\boldsymbol{M}, SOF) \\ 0 & For\ R_{rup} \geq R_{max}(\boldsymbol{M}, SOF) \end{cases} \tag{9b}$$

where φ_{Red} is the modeled reduction of the within-event standard deviation. The coefficient $e_1(\mathrm{T})$ is listed in Table 4-4, where e_1 for periods between those listed in the table can be calculated using a linear interpolation in $\ln(\mathrm{T})$ space.

The standard deviation adjustment model is appropriate over the period range 0.01 to 10 seconds, in the magnitude range **M**5.0-8.0, and only applies for sites within the footprint of the directivity model (e.g. for rupture distances less than R_{max}; this is built into Equation 9b). This model is developed as described in Section 5.5.

Table 4-4. Period dependence of e_1

T (sec)	0.01	0.2	0.25	0.3	0.4	0.5	0.75	1	1.5	2	3	4	5	7.5	10
e_1	0.000	0.000	0.008	0.020	0.035	0.051	0.067	0.080	0.084	0.093	0.110	0.139	0.166	0.188	0.199

4.5. Assumptions and Limitations

There are several assumptions and limitations associated with the model. The assumptions about the geometry of earthquake ruptures (composed of rectangular segments with horizontal tops and bottoms) are described in Section 3. This formulation, along with use of the GC2 coordinate system, allows application of the model to discontinuous multi-fault ruptures. In this process, the coordinate U is converted to the directivity parameter S, and the simple algorithm for S includes the distance between any disconnected ruptures. Therefore, ruptures with relatively large gaps will experience artificially increased S values in some locations.

The model simplifies the description of multi-segment ruptures. It assumes a given rupture has one primary hypocenter (which must lie in the plane of one rupture segment), and has a characteristic style of faulting, with characteristic rake and dip angles. To apply the model to rupture forecasts, like UCERF3, which have individual ruptures with along-strike variations in style of faulting, rake angle, dip, or with multiple hypocenters requires selecting a characteristic value for each of these parameters. We recommend using the average dip and rake angles weighted by segment (or strand) area, with care being taken regarding these selections (e.g. it may not be appropriate to average two segment rake angles of 0 and 180, especially if these two segments have strike angle differences of about 180). In many cases, the characteristic values may not be averages but should be, for example, values from the primary segment of a two-segment rupture with a smaller conjugate rupture. In the most extreme complex cases, the model may not be applicable; this determination will require user judgement.

Three limitations which existed in previous versions of our directivity model still remain. One, the simple distance taper applied to the directivity effect is not well constrained and is based on observation. We choose a magnitude-dependent maximum distance for this taper (ranging from 40 km at **M**5 to 80 km at **M**7 and higher for strike-slip) based on the observation that the residuals (mostly simulations) were best fit when screening the data based on these ranges. Additionally, we observe that the directivity effects are more concentrated to the near-fault region in the reverse style of faulting simulations than the strike-slip simulations, and model this feature with a simple reduction in the maximum distance of the taper. Spudich and Chiou (2013) note that the distance taper should be a function of period because directivity can be observed at long periods at teleseismic distances, but this behavior is not modeled. Second, there are still relatively few data (including simulations) from reverse and normal faulting ruptures to support the model. A key conclusion about the five directivity models from Spudich et al. (2013) was that, for reverse faults, the assumptions of each model had a stronger effect on the predictions than did the data. This issue persists and will continue until we have more data from reverse and normal faulting earthquakes. Third, the directivity predictors used by the model are ad-hoc and intuitive in nature, and although they appear to work well, this also means that for scenarios (e.g. magnitudes, styles of faulting, periods, source-site azimuths, etc) with little data, the model is strongly based on the assumptions about the behavior of these predictors.

The model classifies ruptures into two categories: predominantly strike-slip ruptures ($SOF = 1$) and all other (reverse, normal, and oblique; $SOF = 2$). The intention of this classification is to capture the differences observed in a predominantly strike-slip rupture, where we assume the rupture is bilateral and travels approximately parallel to the ground surface in both directions, and in a rupture which is predominantly traveling from some depth upward towards the ground surface. In the strike slip case, the bilateral assumption of the rupture means that forward directivity effects are modeled, to some degree, at either end of the rupture from the hypocenter. In forward application, this has the potential to over-estimate the ground motion amplification in the case of a unilateral rupture. In the reverse faulting case, up-dip rupture propagation is assumed, and as a result only sites in the up-dip direction from the hypocenter (usually near the fault trace) are modeled to experience forward directivity effects. This results in substantially different patterns of the expected effect compared with the strike-slip model (e.g. Section 6.1).

In both categories, our directivity model assumes that the earthquake rupture is, to some degree, propagating in the same direction as the slip. (The two conditions for forward rupture directivity are rupture front propagation toward the site and slip in the same direction). In reality, the direction of rupture propagation and its consistency with the slip direction will affect the degree of rupture directivity (Aagaard et al., 2004).

A user has the option to specify the style of faulting category, or else the category will be automatically selected based on the characteristic rake angle provided. In the rake-based categorization, $SOF = 1$ is applied for the following characteristic rake angles, in degrees: -30 $\leq$ Rake $\leq$ 30, -180 $\leq$ Rake $\leq$ -150, and 150 $\leq$ Rake $\leq$ 180. A limitation of this approach is that the model does not predict a smooth transition in amplifications for a given rupture at the transition between these categories. For example, a scenario with Rake=30 degrees will have a considerably different f_G map than the same scenario with Rake=31 degrees if the rake angle is used to determine the style of faulting. However, if the user specifies the style of faulting (either $SOF = 1$ or $SOF = 2$) in both of these examples, then the transition will be smooth. Therefore, the user should take care to select the appropriate characteristic rake or should specify the style of faulting when appropriate.

Finally, a few of the least-squares fits upon which the model is based are not very robust; especially those for b_{max} and f_{G0} as a function of **M**. The cause of these may be that both variables have errors. In a future model update, we will consider a regression that accounts for errors in both the horizontal (abscissa) and vertical (ordinate) axis parameters.

5. Detailed Approach

5.1. Simulations

There is a rich quantity of simulated ground motions available due to modern research advances in the areas of numerical computing, geodynamics and seismology. The abundant quantity of simulations made available by researchers span a vast range of techniques, wave propagation methods, breadth, assumptions, scenarios, and magnitudes. We utilize the results from a selection of vetted simulation methods spanning a range of these. Table C-1 (Appendix C) lists the twelve sets of simulations that we considered to be high quality, technically defensible, and valuable for constraining our directivity model.

In selecting the simulations, we gave preference to those performed using 1D seismic velocity models instead of 3D models. 3D simulations can introduce basin effects in the ground motions, which manifest as spatially clustered patches of amplification (or relative de-amplification outside of basins). The GMMs do not capture these effects well if the basin depth terms are not well-constrained. Because the model is developed from GMM residuals, these patches of amplification due to 3D basin effects degrade the analysis. With 1D simulations, these basin effects are not encountered. 1D simulations performed for a reference site condition are also desirable for our purposes, because the near-surface Vs30-based amplification does not need to be corrected for. Nine of the twelve simulations used are 1D. A description of each simulation method is given in Appendix C.

The procedure taken to analyze for directivity effects is comparable for each simulation. Figures are provided in this section for the Graves (2009) simulation of the 1906 **M**7.8 San Francisco earthquake (Set 8 in Table C-1) to illustrate the procedure. Similar figures for the other simulations can be found in Appendix C.

For each simulation scenario, we collect the synthetic waveforms, collect or calculate the metadata (GMM input parameters like distance, site conditions, etc.) and calculate within-event residuals from three NGA-West2 GMMs: Abrahamson et al. (2014), Boore et al. (2014), and Campbell and Bozorgnia (2014). We also calculate the mean residual from these three GMMs. For brevity, we refer to the mean residual from these three GMMs as the ABC14 average. Then, we calculate the GC2 coordinates for the simulation stations corresponding to these ground motions. Figure 5-1 shows an example of these two steps for Simulation Set 8.

At a set of periods (T= 0.01, 0.03, 0.05, 0.10, 0.30, 0.50, 1.0, 1.5, 2.0, 3.0, 4.0, 5.0, 7.5, and 10.0 sec) we analyze the trends in residuals. First, the trends versus the basic GMM predictor variables Rrup and Vs30 are checked to verify that no strong trends or biases exist versus these parameters. The residuals are then examined versus the relevant directivity parameters and directivity predictor functions (defined in Table 4-1); for this strike-slip case $S2$, θ, f_{S2}, f_θ and f_G (Figure 5-2).

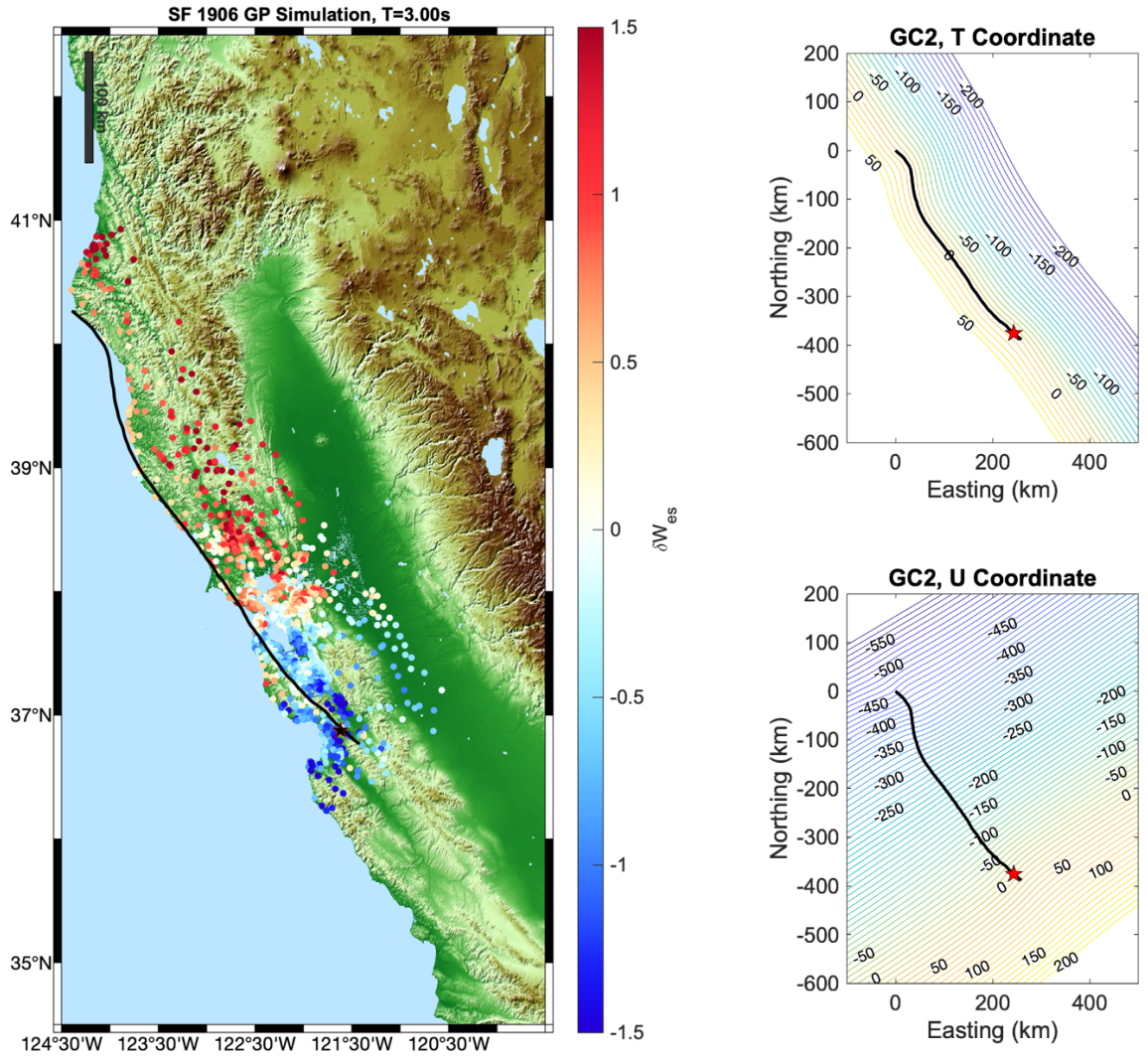

Figure 5-1. Left: Simulation Set 8 mapped within-event residuals (colored circles) at T=3 sec (ABC14 average). The rupture trace is given by the black line and the hypocenter is given by the star. The colored background (topography) is shown to give a sense of scale and location. Right: Mapped GC2 coordinates for a grid covering the range of simulation stations.

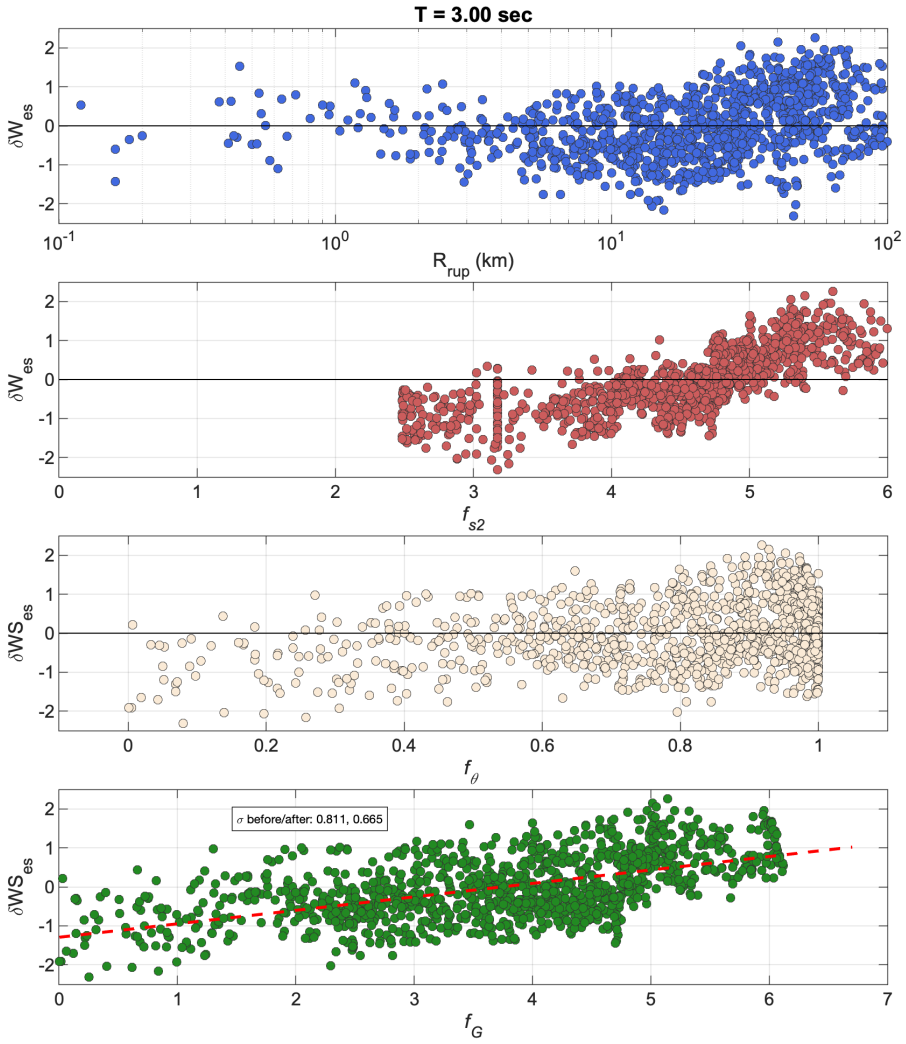

Figure 5-2. Simulation Set 8 within-event residuals (colored circles) at T=3 sec (ABC14 average) versus various parameters. In the bottom panel, the standard deviation of these within-event residuals is given, as calculated before and after the candidate directivity adjustment is applied (red line).

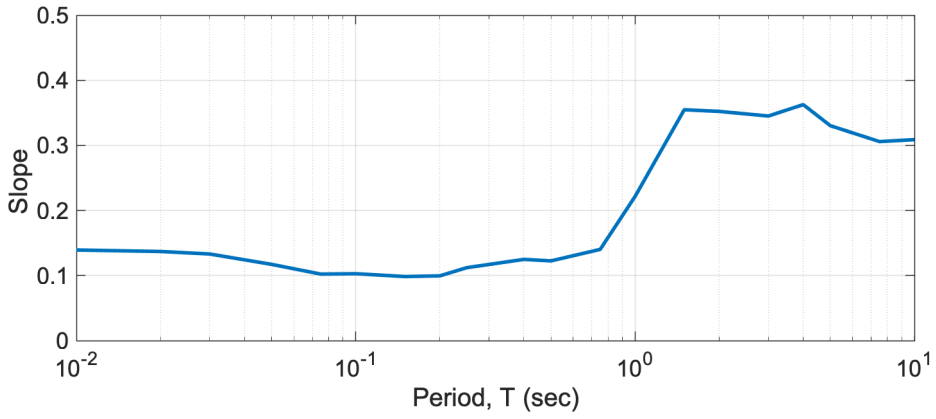

Figure 5-3. Period dependence of the slope of the linear trend in within-event residuals versus f_G.

The directivity effect for this scenario and spectral period is quantified by a linear least squares regression, where the directivity predictor, f_G is the independent variable and the within-event residual is the dependent variable (red dashed line in Figure 5-2). The slope of this linear regression is tracked for each period; we denote this coefficient b (Figure 5-3) In addition to the slope, the y-intercept and standard errors in both coefficients are estimated. With the best-fit slope and y-intercept, the x-intercept is also defined for a linear relationship. We denote the x-intercept as f_{G0} because it is the value of f_G for which the directivity effect is, on average, zero.

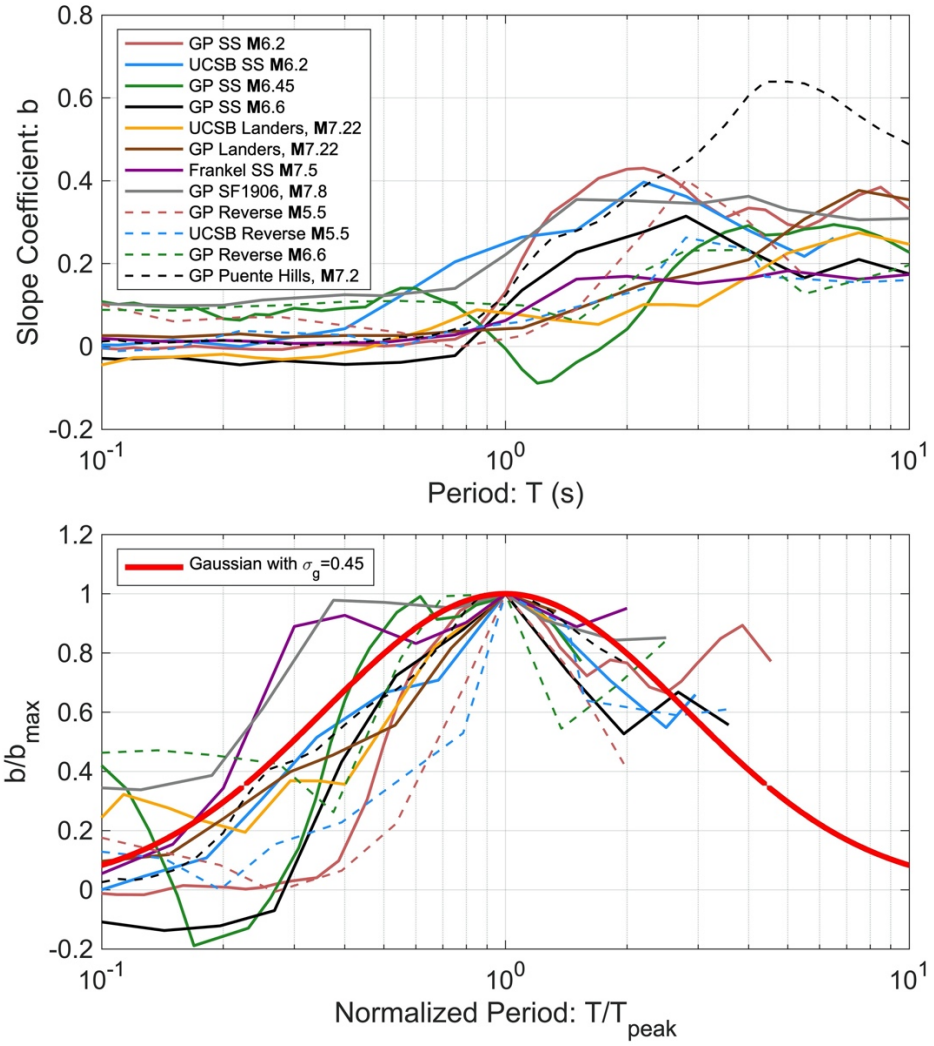

Figure 5-4. A summary of the simulation-based results. Top: The period dependence of slope b. Bottom: Bandwidth of b, and a Gaussian function with best-fit standard deviation parameter $\sigma_g = 0.45$.

As described previously, this procedure is repeated for each of the 12 simulation scenarios. From this stage, we follow the technique of Spudich and Chiou (2013) to develop an ad-hoc directivity model. Figure 5-4 shows the period dependence of b for the simulations. To investigate the bandwidth of b, each curve in the top panel of Figure 5-4 is normalized by its maximum b value (b_{max}) and the periods are normalized by the period

corresponding to b_{max} (T_{peak}). A Gaussian function is fit to these results (red line in the bottom panel of Figure 5-4), where the only free parameter is the standard deviation of the Gaussian, σ_g (Equation 10, noting the similarity to Equation 2b).

$$\frac{b}{b_{max}} = \exp\left(\frac{-[\log_{10}\left(\frac{T}{T_{peak}}\right)]^2}{2\sigma_g^2}\right) \quad (10)$$

In addition to fitting the set of 12 normalized curves, each is also fit to a Gaussian function to determine the estimate of σ_g for each simulation. There is some evidence for magnitude dependence of the bandwidth (the largest two event-based values of σ_g come from the two largest magnitude simulations), although we elect not to model this feature because the data do not support it (Section 5.2). The parameter estimates for each simulation are given in Table 5-1.

Table 5-1. Estimates of b_{max}, T_{peak}, f_{G0}, and σ_g for the 12 simulations evaluated, sorted by **M**.

Simulation	**M**	Table C-1 Set #	b_{max}	b_{max} std error	T_{peak}	f_{G0}	σ_g
GP Reverse	5.5	9	0.40	0.0138	2.0	1.07	0.21
UCSB Reverse	5.5	11	0.26	0.0300	2.8	1.07	0.37
GP Strike-Slip	6.2	1	0.43	0.0080	2.2	1.34	0.56
UCSB Strike-Slip	6.2	2	0.40	0.0189	2.2	1.33	0.39
GP Strike-Slip	6.45	3	0.29	0.0136	6.5	1.54	0.42
GP Strike-Slip	6.6	4	0.31	0.0095	2.8	1.63	0.38
GP Reverse	6.6	10	0.23	0.0128	4.0	1.40	0.55
GP Puente Hills	7.2	12	0.64	0.0179	5.0	1.91	0.38
GP Landers	7.22	5	0.38	0.0089	7.5	2.15	0.34
UCSB Landers	7.22	6	0.27	0.0076	7.5	2.15	0.32
Frankel Strike-Slip	7.5	7	0.18	0.0126	10.0	3.03	0.62
GP SF 1906	7.8	8	0.36	0.0148	4.0	3.75	0.62

The weak magnitude dependence of b_{max} is evident in the top panel of Figure 5-5. In this figure, we also show the least squares line of best fit (grey line). Similarly, the top panel of Figure 5-5 shows the much stronger observed magnitude dependence of f_{G0} (the value of f_G for which the average directivity effect is zero) in blue. The blue solid line is the least squares line of best fit to the strike-slip simulations, and the blue dashed line is the same for reverse faulting simulations.

The observed magnitude dependence in f_{G0} is not necessarily intuitive. This feature is the result of working with within-event residuals, as opposed to modeling an absolute directivity effect. For an absolute directivity effect, we would not expect that the value of f_G (or, more simply, the value of S) corresponding to zero directivity effect would change with magnitude. However, in working with centered residuals, the model is fitting an adjustment to an existing ground motion prediction. Therefore, the model is self-centered, meaning that it predicts both amplification and de-amplification adjustments. Because the

range of possible f_G values is controlled by the dimensions of the rupture, it follows that f_{G0} must scale with magnitude to allow for this self-centering.

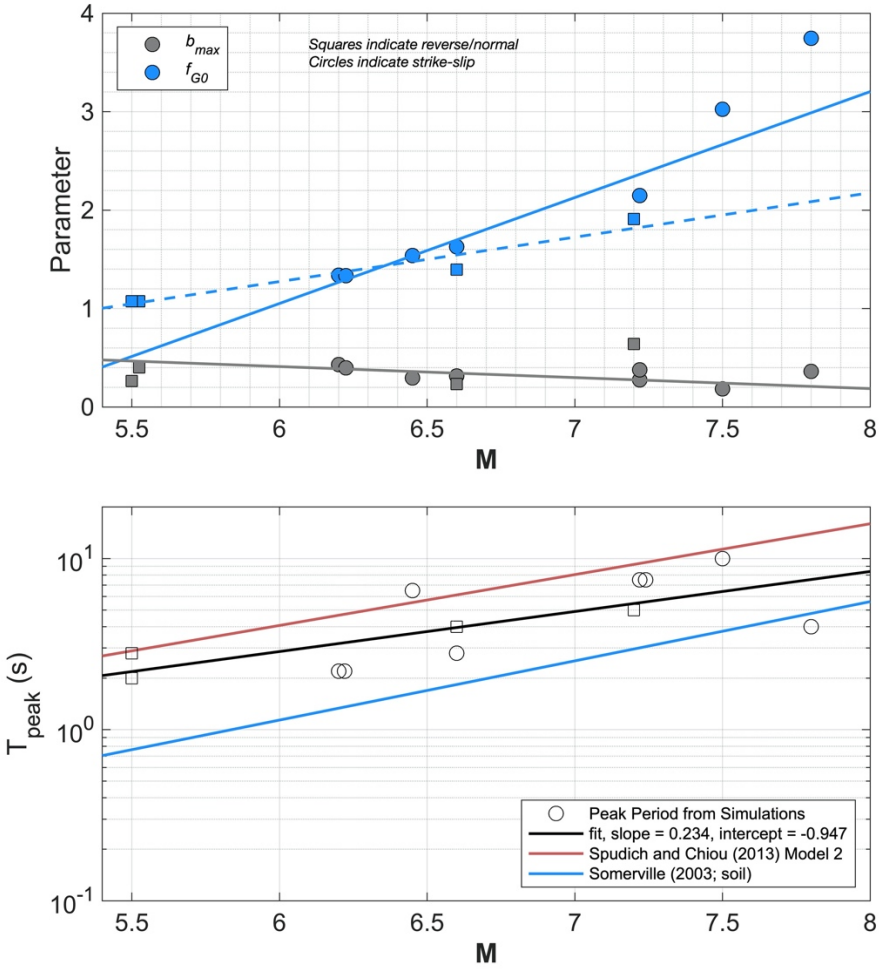

Figure 5-5. A summary of the simulation-based results. Top: The magnitude dependence of slope b_{max} and f_{G0}. Bottom: The magnitude dependence of T_{peak}.

The relationship between magnitude and $\log_{10} T_{peak}$ is developed as shown in the bottom panel of Figure 5-5, where the white symbols represent T_{peak} of the simulations and the black line is the least squares line of best fit. There is not evidence to support separate relationships based on the style of faulting. For comparison, this figure also shows the Spudich and Chiou (2013) relationship for the period of peak IDP effect derived from NGA-West2 data, and the Somerville (2003) relationship for the velocity pulse period, which was estimated in the time domain, possibly explaining its difference from the other relationships.

The coefficients of the linear relationships for b_{max}, $\log_{10} T_{peak}$, and f_{G0} are used to model the magnitude and period dependence of model coefficients $a(\boldsymbol{M},T)$ and $b(\boldsymbol{M},T)$ (Equation 1). These model coefficients are not listed because this model is only used to inform and compare with the model developed in subsequent stages. Because our

approach follows the Spudich and Chiou (2013) algorithm for modeling the magnitude- and period-dependence of the directivity effect, Equation 1 is similar to Equation 5.1a of Spudich et al. (2013). The key differences are the use of the f_G directivity predictor instead of IDP, the magnitude-dependence of f_{G0} as a centering mechanism, and the use of the simulations to constrain the ad-hoc model.

5.2. NGA-W2 Data

As described in Section 3, we evaluate the residuals from the NGA-West2 database, using the same three GMMs, and for the earthquakes with a finite fault model and at least five recordings. The procedure we take is similar to the one described in Section 5.1, except using within-event residuals from the data rather than from the simulations. Of course, the azimuthal coverage of the recorded data is generally much sparser than the simulations. This leads to issues in the residual analysis when there is not enough coverage to sample both forward and backward rupture directivity zones, because we might expect an event with sites only in a forward directivity zone to have positive residuals, but by definition the within-event residuals are zero-centered. Because of this problem, the events with few data, and those with poor azimuthal coverage, are not very helpful in constraining the model. Nevertheless, all of the events with a finite fault model are worth examination. Ultimately, we use the 21 events listed in Table 5-2. Maps of residuals and figures showing trends of residuals with the directivity predictors for all events can be found in Appendix D.

Figure 5-6 shows the period dependence of b obtained from analysis of the within-event data residuals. Figure 5-7 displays the Gaussian function fit to the normalized b values, as well as the magnitude dependence of b_{max}, T_{peak}, and f_{G0}.

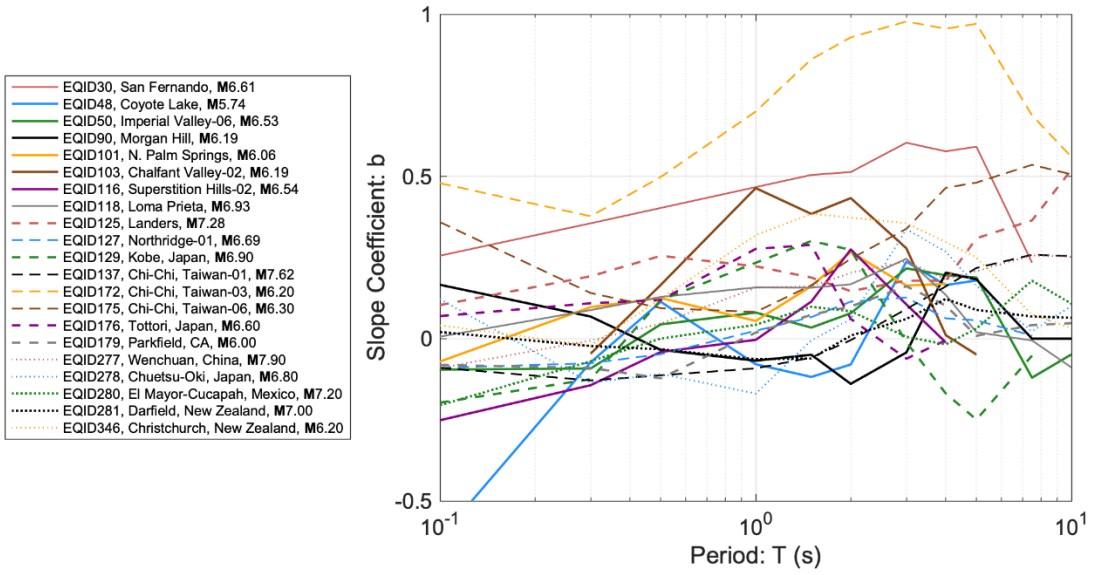

Figure 5-6. The period dependence of slope b obtained from the residual analysis of data from 21 NGA-W2 earthquakes.

Table 5-2. Estimates of b_{max}, T_{peak}, f_{G0}, and σ_g for the 21 earthquakes evaluated.

Earthquake	Style of Faulting	M	b_{max}	b_{max} std error	T_{peak}	f_{G0}	σ_g
EQID48, Coyote Lake	Strike-slip	5.74	0.24	0.1657	3.0	0.75	0.60
EQID179, Parkfield, CA	Strike-slip	6	0.16	0.0762	3.0	1.73	0.20
EQID101, N. Palm Springs	Strike-slip	6.06	0.27	0.1538	2.0	1.66	0.47
EQID90, Morgan Hill	Strike-slip	6.19	0.20	0.0753	4.0	2.87	0.21
EQID103, Chalfant Valley-02	Strike-slip	6.19	0.46	0.1524	1.0	1.14	0.39
EQID172, Chi-Chi, Taiwan-03	Reverse	6.2	0.98	0.0802	3.0	0.48	0.58
EQID346, Christchurch, NZ	Oblique	6.2	0.39	0.1334	1.5	0.50	0.58
EQID175, Chi-Chi, Taiwan-06	Reverse	6.3	0.54	0.0463	7.5	1.02	0.45
EQID50, Imperial Valley-06	Strike-slip	6.53	0.22	0.0882	3.0	2.38	0.28
EQID116, Superstition Hills-02	Strike-slip	6.54	0.28	0.1975	2.0	1.73	0.11
EQID176, Tottori, Japan	Strike-slip	6.6	0.29	0.1057	1.5	1.84	0.43
EQID30, San Fernando	Reverse	6.61	0.60	0.1234	3.0	0.46	0.36
EQID127, Northridge-01	Reverse	6.69	0.13	0.0396	3.0	0.95	0.22
EQID278, Chuetsu-Oki, Japan	Reverse	6.8	0.34	0.1627	3.0	0.20	0.18
EQID129, Kobe, Japan	Strike-slip	6.9	0.30	0.0832	1.5	2.38	0.35
EQID118, Loma Prieta	Oblique	6.93	0.25	0.0933	3.0	2.15	0.54
EQID281, Darfield, NZ	Strike-slip	7	0.12	0.0696	4.0	2.50	0.27
EQID280, El Mayor-Cucapah, Mexico	Strike-slip	7.2	0.18	0.0528	7.5	2.23	0.54
EQID125, Landers	Strike-slip	7.28	0.52	0.1267	10.0	2.51	0.32
EQID137, Chi-Chi, Taiwan-01	Oblique	7.62	0.26	0.0325	7.5	1.21	0.28
EQID277, Wenchuan, China	Oblique	7.9	0.26	0.0604	7.5	1.42	0.80

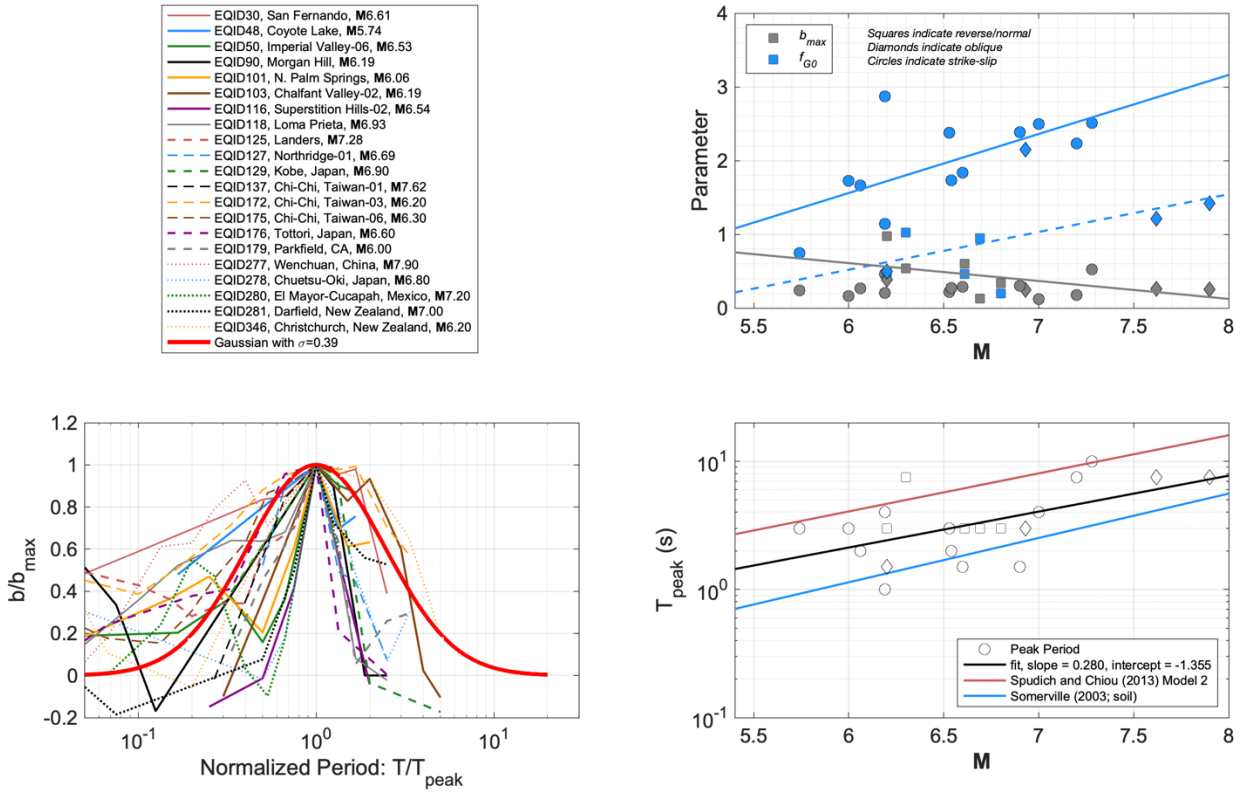

Figure 5-7. Results for the 21 NGA-W2 events analyzed. Top: The magnitude dependence of slope b_{max} and f_{G0}. Left: Bandwidth of b, and a Gaussian function with best-fit standard deviation parameter $\sigma_g = 0.39$ Right: The magnitude dependence of T_{peak}.

5.3. *Composite Result*

The combined database (simulations and data) estimates of b, b_{max}, T_{peak}, and f_{G0} are used to develop an ad-hoc composite model, as shown in Figure 5-8. This model serves as a comparison for the regression-based model developed in the next step.

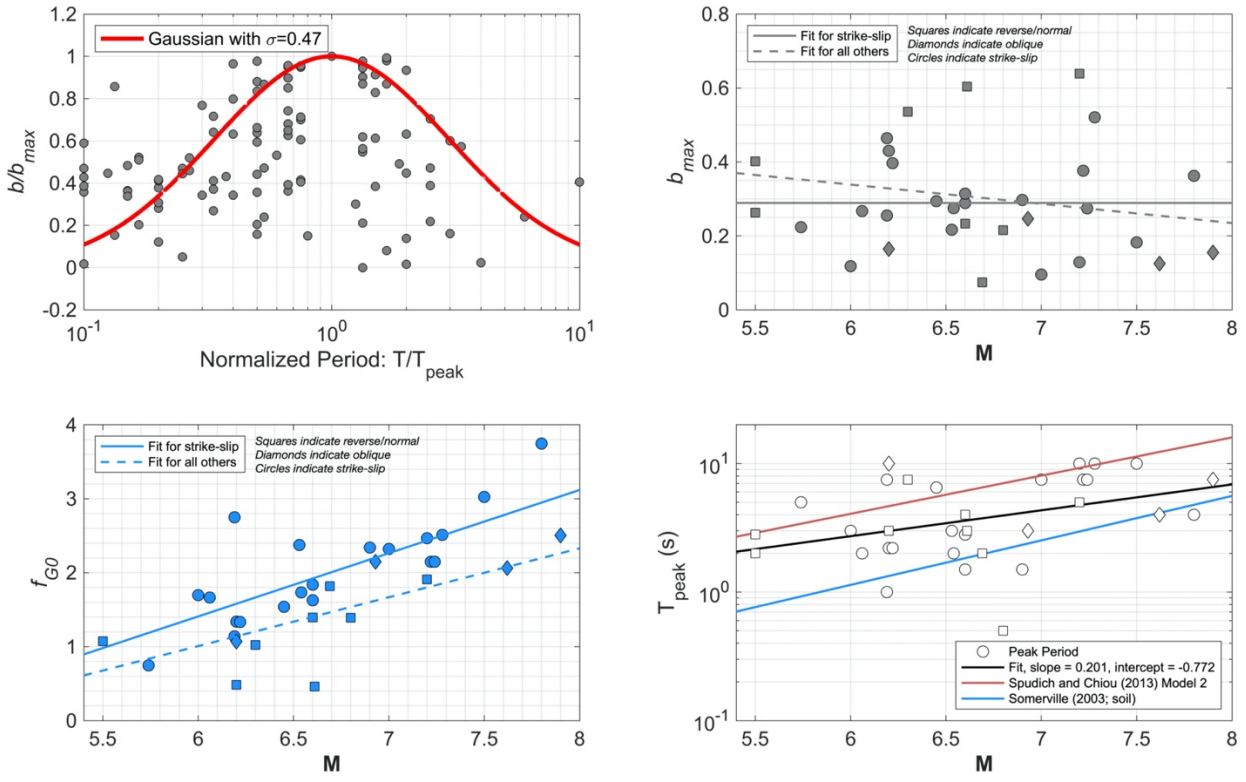

Figure 5-8. Results from the combined database of estimated parameters, including the Gaussian function with best-fit standard deviation parameter $\sigma_g = 0.47$, and the magnitude dependence of b_{max}, f_{G0}, and T_{peak}.

5.4. *Final Model: Regression*

A nonlinear least squares regression is performed using the combined database of within-event residuals (simulations and data) to derive the final model coefficients: $b_1, b_2, c_1, c_2, d_1, d_2$, and σ_g. As identified by Spudich and Chiou (2013), the coefficients are independent of period, therefore they are estimated in a regression with combined residual data of all periods; doing so ignores any correlation in the residuals between periods (Spudich and Chiou, 2013). The coefficients are listed in Table 4-2. The resulting models for b_{max}, T_{peak}, and f_{G0} are shown in Figure 5-9, where this figure is the same as Figure 5-8, except with the final (regression) models shown in green.

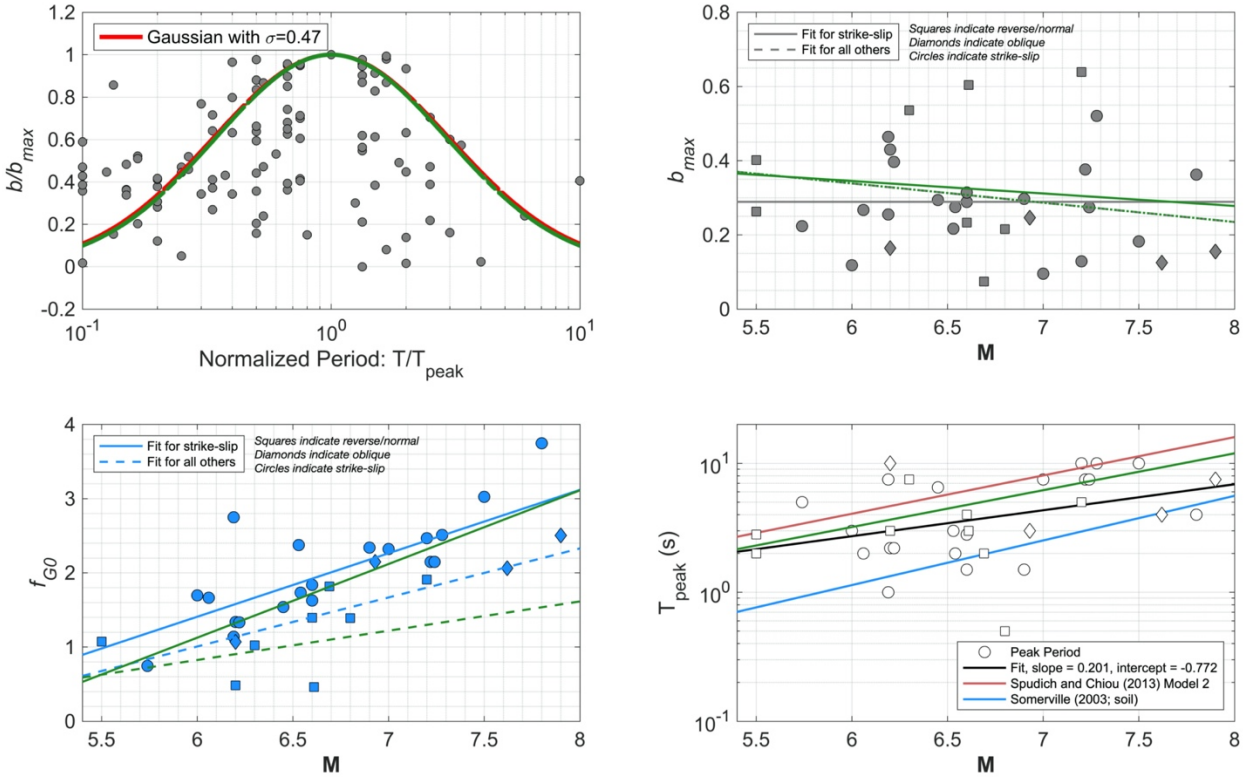

Figure 5-9. The same as Figure 5-8, but with the final (regression) models shown in green.

5.5. *Aleatory Variability*

Using the final model coefficients, the within-event residuals of the NGA-W2 data (from the same three GMMs as in previous analyses) are adjusted for median directivity effects. We calculate φ before and after this adjustment for all of the NGA-West2 events with a finite fault model. In these calculations, stations are included only if they are within the distance range for which the model predicts directivity adjustments (e.g. for rupture distances less than R_{max}, which varies with **M** and the style of faulting, Equation 3e). At both stages, we inspect the within-event residuals versus rupture distance and the directivity adjustment, f_D, as shown in Figure 5-10, where the red circles are the residuals after applying the directivity median adjustment. The purpose of this evaluation is to confirm that the distance scaling is not adversely affected, and to visualize the effect of the directivity model, which reduces the residuals for positive values of f_D, and increases them for negative f_D. In the case of the Wenchuan earthquake (T=5 sec), application of the model reduces φ as indicated in the bottom panel of Figure 5-10.

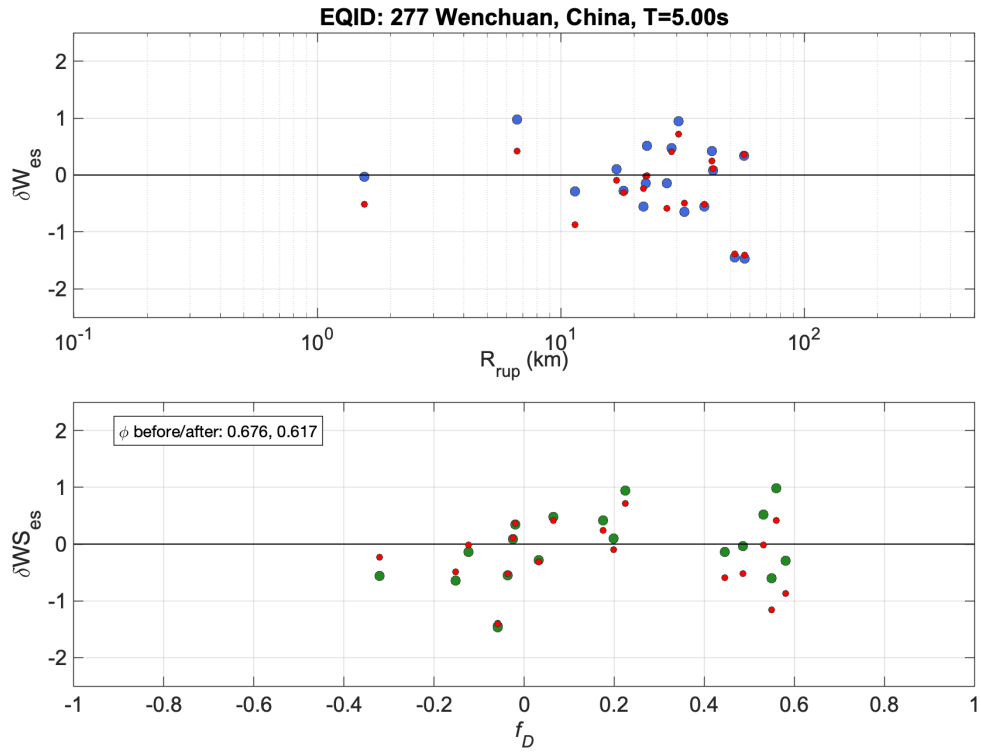

Figure 5-10. The effect of applying the directivity adjustment model on Abrahamson et al. (2014) within-event residuals for the Wenchuan, China earthquake, considering sites within R_{max} = 60 km rupture distance, at T=5 sec. Blue and green circles are the residuals before the adjustment, and red circles are after.

Table 5-3 summarizes the event-based standard deviations at T=5 sec, using the ABC14 average residuals. This summary is used to evaluate which events, in terms of their GMM residuals, support the directivity model. The residuals from certain events do not agree with the model. This could be because the directivity effects are not strongly expressed in the residuals, because the model is not accurately capturing directivity effects, or for

some other unidentified reason. Comments are provided in Table 5-3 for events with obvious explanations. The most common obvious causes for poor agreement are scarcity of data or lack of azimuthal variations in the data, both of which skew the apparent directivity effect because the within-event residuals are centered. For example, if an earthquake has recording stations located only within a zone of strong expected directivity amplification, but these residuals are already centered on zero, then applying the directivity adjustment to the residuals is likely to increase φ. The same principle applies for an earthquake with very few recordings. Excluding these, there are 16 events which enjoy reduced φ upon application of the directivity model (highlighted in green) and 6 which suffer increases in φ but do not have a clear cause for exclusion (red). These 22 events are used for the remainder of the variability analysis.

Table 5-3. Earthquake-based within-event standard deviations at T=5 sec.

Earthquake	EQID	**M**	φ_{NoDir} T=5 sec	φ_{Dir} T=5 sec	φ_{Red} T=5 sec	# of sites	Supports Model?
San Fernando	30	6.61	0.695	0.463	0.519	6	Y
Tabas, Iran	46	7.35	1.272	1.024	0.754	2	Y; limited data
Coyote Lake	48	5.74	0.365	0.342	0.127	6	Y; limited data
Imperial Valley-06	50	6.53	0.463	0.447	0.122	30	Y
Irpinia, Italy-01	68	6.90	0.294	0.544	-0.458	4	N; limited data
Morgan Hill	90	6.19	0.399	0.388	0.095	11	Y
Nahanni, Canada	97	6.76	0.878	1.297	-0.955	2	N; limited data
N. Palm Springs	101	6.06	0.766	0.759	0.099	5	Y
Chalfant Valley-02	103	6.19	0.459	0.540	-0.284	6	N; limited data
Superstition Hills-02	116	6.54	0.419	0.537	-0.335	5	N; limited data
Loma Prieta	118	6.93	0.540	0.496	0.213	15	Y
Landers	125	7.28	0.595	0.445	0.395	22	Y
Northridge-01	127	6.69	0.473	0.534	-0.246	76	N
Kobe, Japan	129	6.90	0.382	0.587	-0.447	18	N; low azimuthal variation
Kocaeli, Turkey	136	7.35	0.367	0.358	0.082	17	Y
Chi-Chi, Taiwan-01	137	7.62	0.618	0.589	0.189	140	Y
Duzce	138	7.14	0.630	0.669	-0.224	15	N; low azimuthal variation
Manjil, Iran	144	7.37	0.000	0.000	0.000	1	Y; limited long T data
Sierra Madre	145	5.61	0.000	0.000	0.000	1	N; limited data
Joshua Tree, CA	146	6.10	0.395	0.461	-0.238	5	N; limited data
Denali, Alaska	169	7.90	0.602	0.533	0.280	4	Y; limited data
Chi-Chi, Taiwan-03	172	6.20	0.495	0.438	0.230	62	Y
Chi-Chi, Taiwan-04	173	6.20	0.571	0.543	0.176	108	Y
Chi-Chi, Taiwan-05	174	6.20	0.641	0.622	0.155	17	Y
Chi-Chi, Taiwan-06	175	6.30	0.621	0.588	0.197	70	Y
Tottori, Japan	176	6.60	0.483	0.514	-0.174	20	N
Parkfield, CA	179	6.00	0.611	0.630	-0.148	50	N
Niigata, Japan	180	6.60	0.385	0.460	-0.251	33	N
Wenchuan, China	277	7.90	0.676	0.617	0.277	19	Y
Chuetsu-Oki, Japan	278	6.80	0.460	0.482	-0.146	70	N; nearly all sites on hanging wall side (region of low expected direct. effect)
Iwate, Japan	279	6.90	0.576	0.567	0.107	79	Y; T-dependent agreement
El Mayor-Cuc., Mex	280	7.20	0.512	0.597	-0.307	42	N
Darfield, NZ	281	7.00	0.376	0.394	-0.117	34	N
Christchurch, NZ	346	6.20	0.282	0.282	0.008	24	Y

The 6 events with unexplained increase in φ are EQID 127, 176, 179, 180, 280, and 281. Perhaps the most perplexing of these is the Northridge earthquake; it was well-recorded and with a relatively simple source description, has the characteristics of reverse-oblique faulting earthquake we would expect the directivity model to capture, although the rupture propagated diagonally from the southeast to northwest corner, not purely up-dip. To investigate, Figure 5-11 (top row) maps the Northridge within-event residuals (without directivity adjustment) from the three GMMs at T=5 sec. Directly up-dip from the rupture plane, where the model predicts the largest amplifications, the residuals are only modestly positive to the northwest of the top edge of the fault and in some cases negative to the northeast of the top edge of the fault. At all other locations, including to the southeast of the hypocenter in the direction of the LA basin, there is an unsystematic mixture of positive and negative residuals. We conclude that the strong motion recordings of this earthquake, at least collectively in terms of the within-event residuals, do not exhibit strong directivity effects. Therefore, applying the model to the existing within-event residuals over-corrects and causes φ to increase (bottom of Figure 5-11).

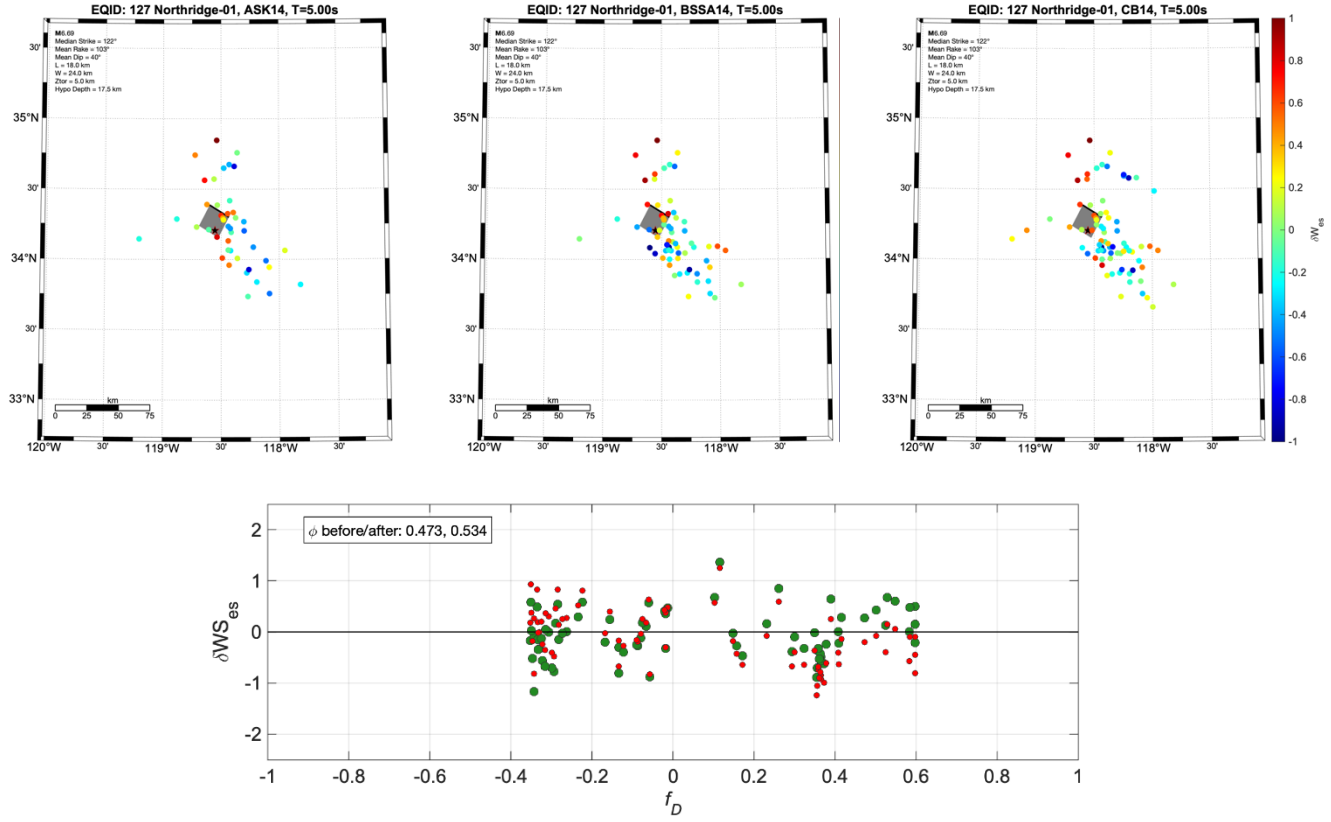

Figure 5-11. Top row: Maps of Northridge within-event residuals from the three GMMs analyzed, at T=5 sec. Bottom: Within-event residuals versus f_D at T=5 sec, showing the over-correction and resulting increase in φ.

For the other five earthquakes with increases in φ, our explanation is similar. Based upon our qualitative observation of ground motion residuals, these events generally don't feature strong spatial coherency. The resulting φ increases, and apparent disagreement

with the model are undesirable, but it is also reassuring that there are not well-defined residual patterns which the model clearly misses. An excellent counter-example to Figure 5-11 is the Chi-Chi, Taiwan mainshock, for which the residuals are mapped in Figure 3-3, and show strong spatial coherence.

The aforementioned set of 22 events are used jointly to calculate φ_{Red} (Equation 9) for the ABC14 average residuals. Figure 5-12 shows an example of the residuals of these events, before and after adjustment, at T=5 sec, along with the φ at each stage. The period dependence of φ_{Red} is shown in Figure 5-13, and the values are listed in Table 4-4.

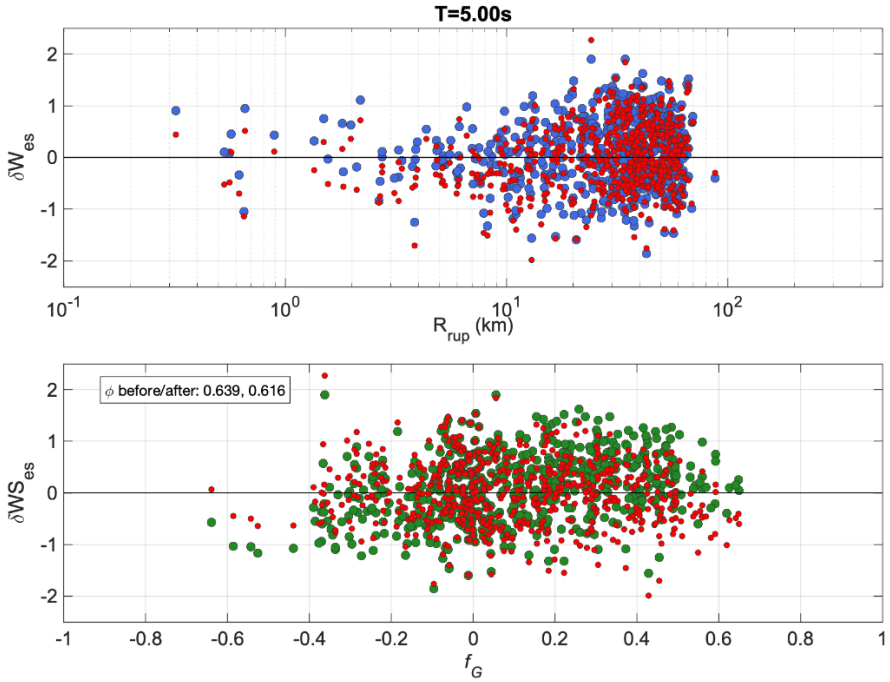

Figure 5-12. The effect of applying the directivity adjustment model to ABC14 within-event residuals of 22 events, at T=5 sec. The top panel shows residuals versus R_{rup} and the bottom versus f_D. Blue and green circles are the residuals before the adjustment, and red circles are after.

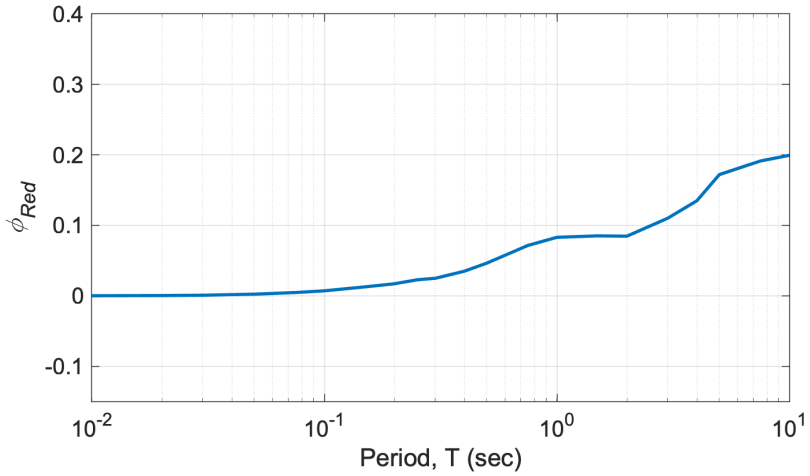

Figure 5-13. The period dependence of φ_{Red}.

6. Examples

6.1. Example 1: Vertical Strike-Slip Scenario (ss3)

This scenario (borrowed from the test scenarios in Table 1.2 of Spudich et al., 2013) is a **M**7.2 vertical strike-slip rupture with rake angle of 180 degrees, and with length of 80 km and down-dip width of 15 km. The hypocenter is located 10 km from the southern end of the rupture, at 10 km depth. The GC2 coordinates for a grid of locations surrounding the earthquake are shown in Figure 6-1. In this simple, straight-rupture case, U is oriented with the y-axis, and the T coordinate is equivalent to the NGA-West2 distance parameter Rx. As required by the directivity model, the origin is the point on the ground surface up-dip from the hypocenter, which coincides with the epicenter in this scenario.

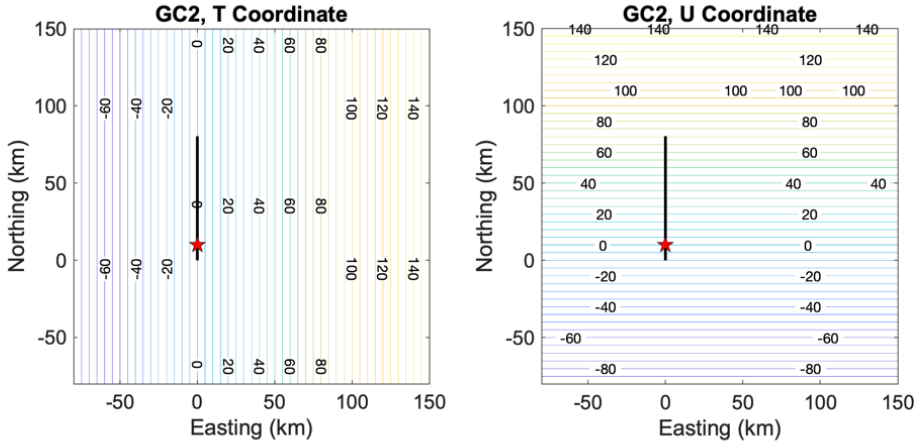

Figure 6-1. GC2 coordinates of the ss3 scenario.

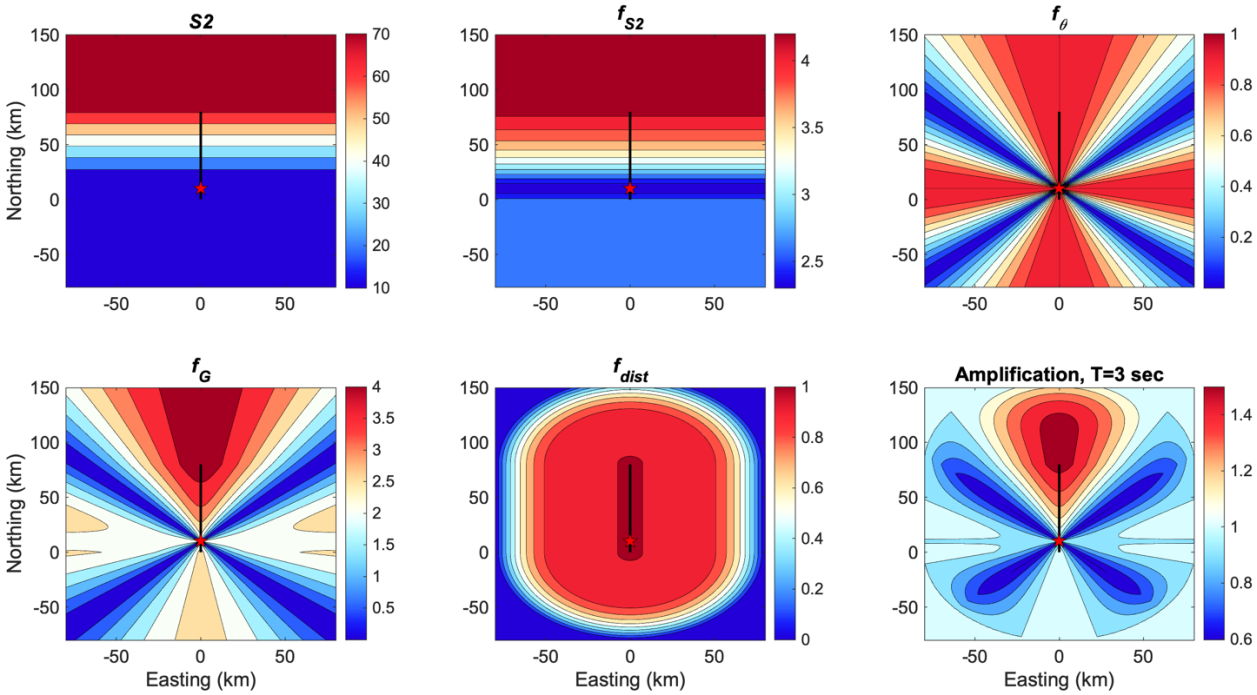

Figure 6-2. Components of the directivity model for the ss3 scenario.

For this first example, each component of the directivity model is shown in Figure 6-2. Starting from the top left panel of Figure 6-2 and moving across, the first panel shows the generalized rupture travel distance parameter, $S2$. The next two panels show the rupture travel distance function, f_{S2}, and the azimuthal predictor function for strike-slip faults, f_θ. Here it can be observed that the amplitude of f_θ mimics the SH radiation pattern lobe for a point-source double couple at the hypocenter. The bottom row shows the period independent geometric directivity predictor, f_G, the distance taper, f_{dist}, and finally the predicted GMM directivity adjustment at T=3 sec, f_D, expressed as amplification $= \exp(f_D)$.

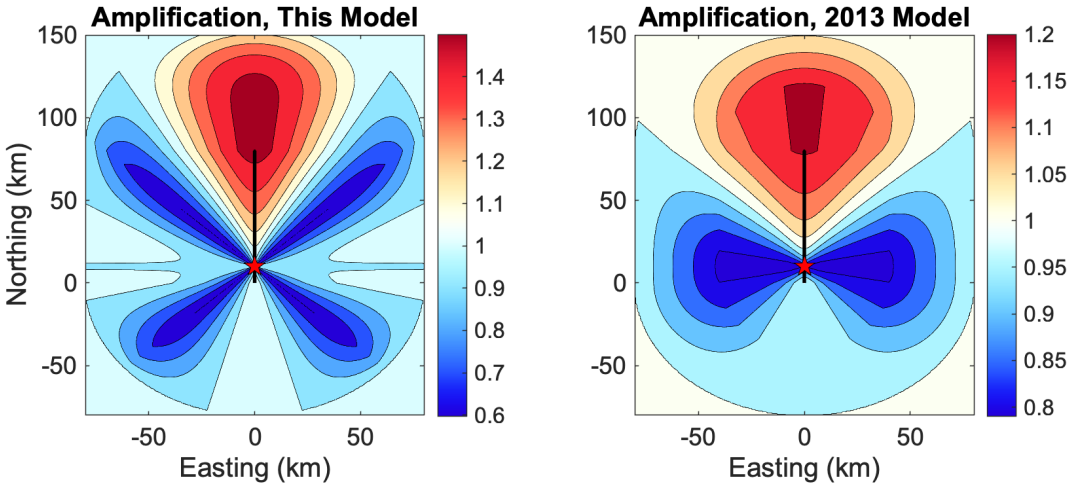

Figure 6-3. Comparison of the T=3 sec amplifications predicted for this scenario between the proposed model (left) and the BS13 model (RotD50 component).

In Figure 6-3, the amplification prediction (T=3 sec) for this scenario is compared with the 2013 model (BS13). Differences in the spatial patterns arise primarily from our improved formulation of f_θ, for which the BS13 model scaled and shifted $\cos(2\theta)$ to range between 0 and 1, and the current model simply takes the absolute value of $\cos(2\theta)$, following SSGA. We consider the current model version to be substantially improved because it better matches the SH radiation pattern lobe. Differences in the maximum and minimum amplifications arise out of the differences in model development, assumptions, and regressions. The BS13 model is broadband, meaning the directivity effect increases with increasing spectral period. The current model is narrowband, and period-dependence of the modeled effect for this scenario is shown in the left hand side of Figure 6-4, where the peak effect for a **M**7.2 rupture is at about T=7 sec. Additionally, the right hand side of Figure 6-4 shows the predicted maximum and minimum amplifications as a function of period for this scenario. In this calculation, the maximum uses $f_G = 4.25 \approx \ln(70)$, where 70 km is the largest possible value of $S2$ for this scenario, and for the minimum, $f_G = 0$, which is the smallest possible value of f_G for any scenario. The corresponding response spectra for a site with $R_{jb} = 0$, with the adjustments applied to the Boore et al. (2014) GMM, are shown in Figure 6-5.

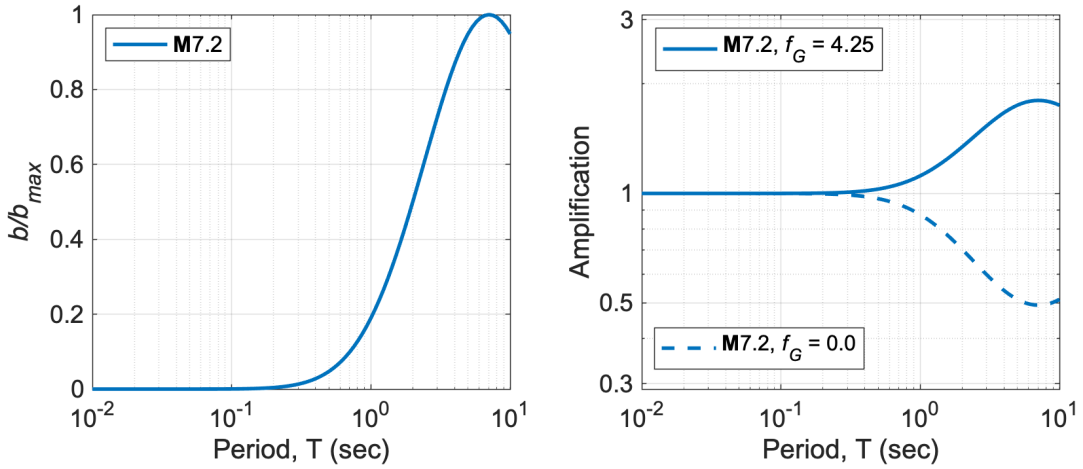

Figure 6-4. Left: Period dependence of b/b_{max} (Equation 2b) for the ss3 scenario. Right: Period dependence of the minimum and maximum predicted amplifications for the ss3 scenario.

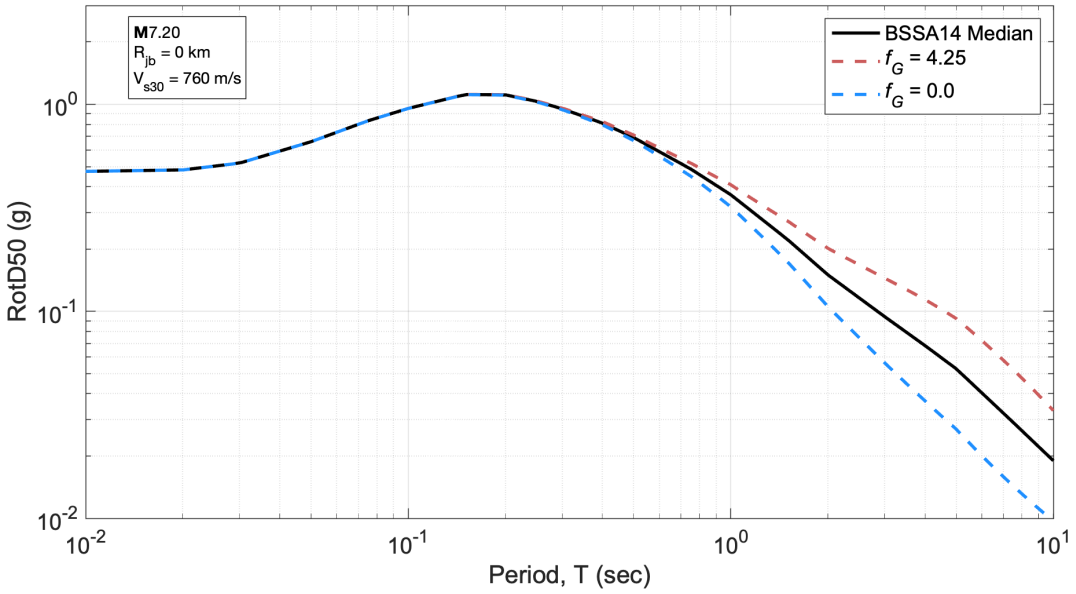

Figure 6-5. Median response spectra predictions using BSSA14, showing the prediction for a site located directly on the fault without directivity adjustment (black line), and with the minimum and maximum predicted directivity adjustment for this scenario (colored dashed lines).

6.2. Example 2: Reverse Faulting Scenario (rv4)

This scenario, also borrowed from Table 1.2 of Spudich et al., (2013) is a **M**7.0 purely reverse-faulting rupture (rake angle of 90 degrees), with strike of 0 degrees, dip angle of 30 degrees, with length of 32 km, down-dip width of 28 km, rupture reaching the ground surface. The hypocenter is located 8 km from the southern end of the rupture, at 10 km depth, which is 20 km down dip from the surface trace. The GC2 coordinates for a grid of locations surrounding the earthquake are shown in Figure 6-6.

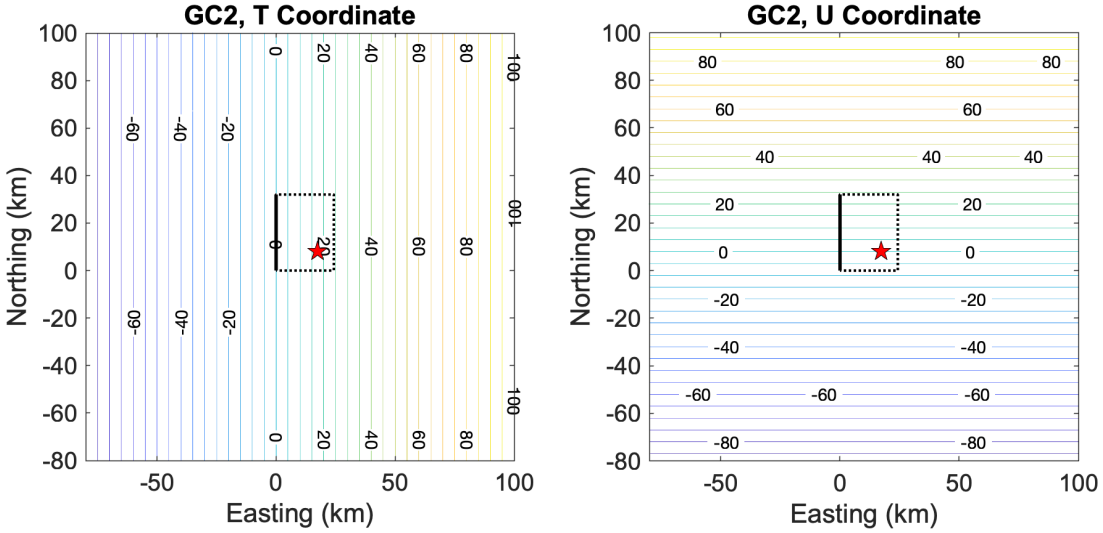

Figure 6-6. GC2 coordinates of the rv4 scenario.

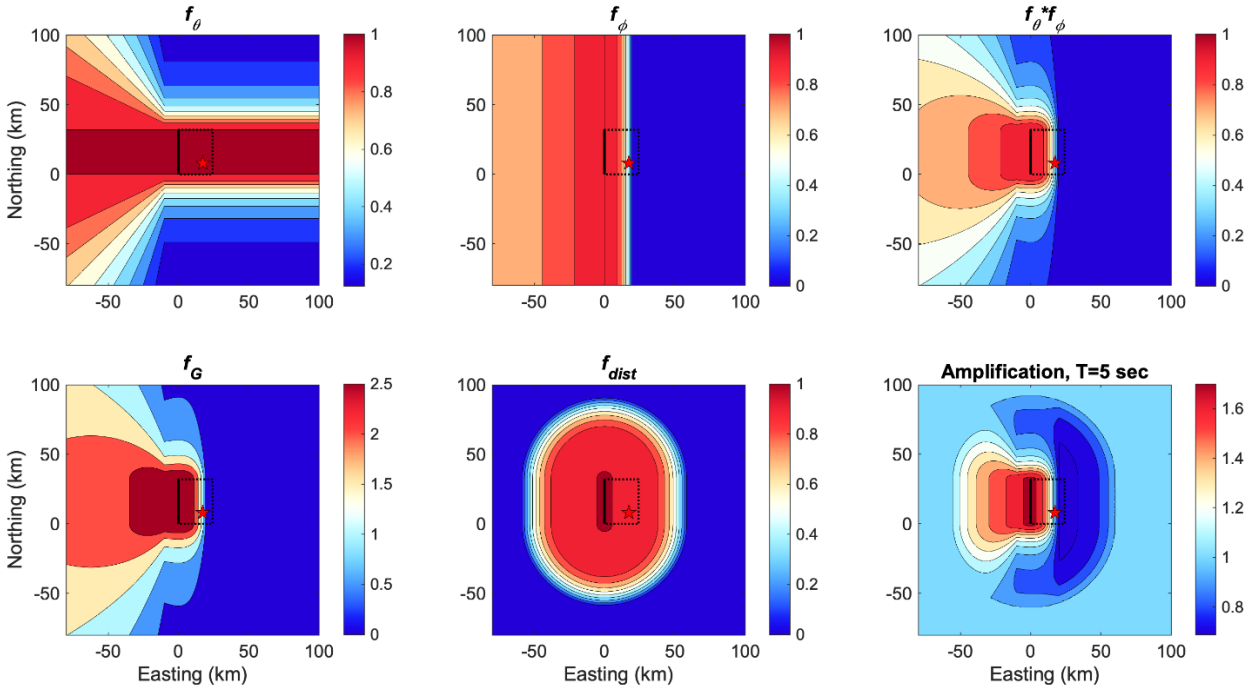

Figure 6-7. Components of the directivity model for the rv4 scenario.

Each component of the directivity model for scenario rv4 is shown in Figure 6-7. The parameter $S2$ is not shown here because this value is constant for all sites; for a purely reverse faulting earthquake $S2$ simplifies to D (Equation 4b). The top row of Figure 6-7 shows the azimuthal predictor function for strike-slip faults, f_θ, f_ϕ, and their product. The bottom row shows the period independent geometric directivity predictor, f_G, the distance taper, f_{dist}, and finally the predicted GMM directivity adjustment at T=5 sec, f_D, expressed as amplification $= \exp(f_D)$.

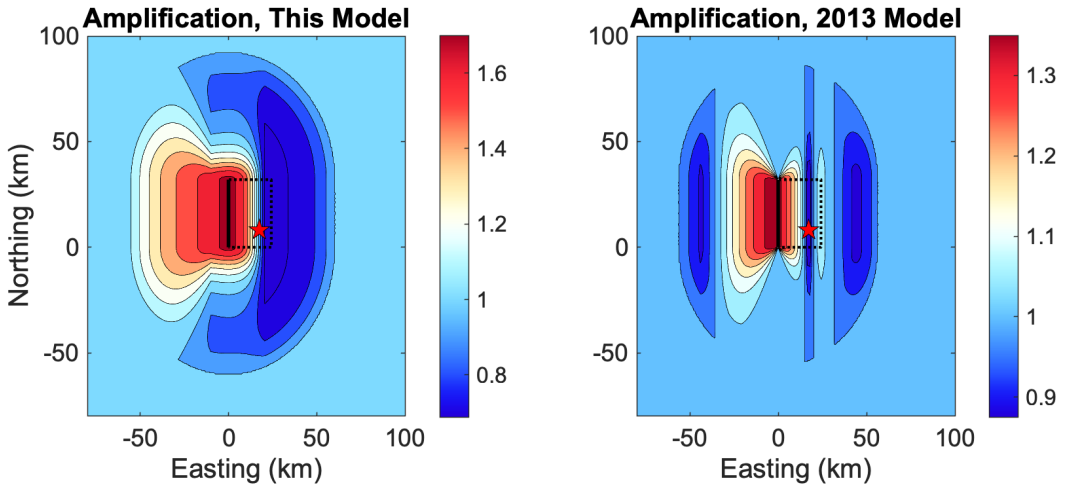

Figure 6-8. Comparison of the T=5 sec amplifications predicted for scenario rv4 between the proposed model (left) and the BS13 model (RotD50 component).

In Figure 6-8, the amplification prediction (T=3 sec) for this scenario is compared with the 2013 model (BS13). The differences in the spatial patterns arise primarily from our improved formulation of $S2, f_\theta$ and f_ϕ. A key difference is in the definition of D, which we define to be measured from the hypocenter to the shallowest depth of the rupture plane, up-dip. Therefore, this parameter takes on the same value for every site on the ground surface. BS13 defined this parameter as the portion of the fault width rupturing toward a site. The latter definition leads to the narrow zones of de-amplification seen in the right-hand side of Figure 6-8. We consider the current model version to be substantially improved because it is simpler and does not cause these zones. Instead, our predictor function f_ϕ models the expected decrease in the directivity effect with increasing Rx. Our predictor function f_θ replaces the azimuth angle taper of BS13. Differences in the maximum and minimum amplifications arise out of the differences in model development, assumptions, and regressions.

The narrowband scheme of the model for this scenario is shown in the left hand side of Figure 6-9, where the peak effect for a **M**7.0 rupture is at about T=6.2 sec. The right hand side of Figure 6-9 shows the predicted maximum and minimum amplifications as a function of period for this scenario. In this calculation, the maximum uses $f_G = 3.0 \approx \ln(20)$, where 20 km is D for this scenario, and for the minimum, $f_G = 0$, which is the smallest possible value of f_G for any scenario.

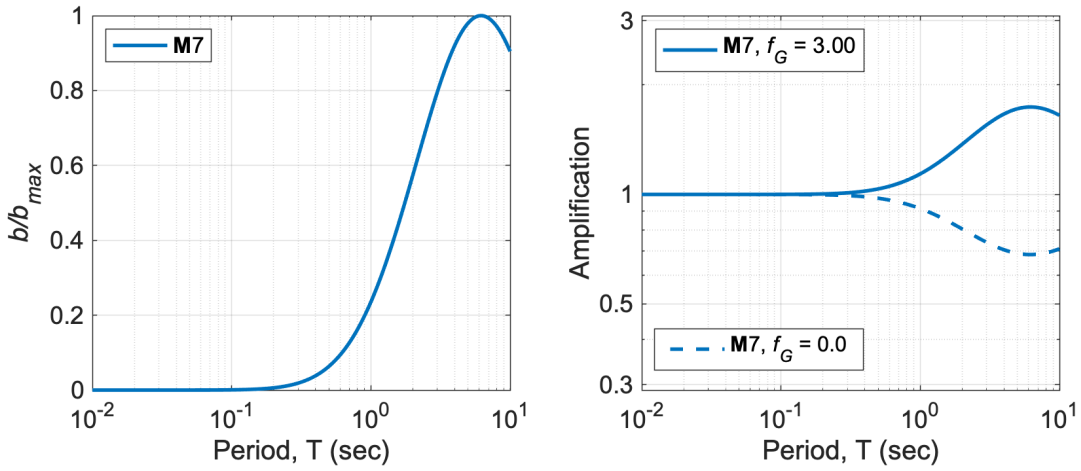

Figure 6-9. Left: Period dependence of b/b_{max} (Equation 2b) for the rv4 scenario. Right: Period dependence of the minimum and maximum predicted amplifications for the rv4 scenario.

6.3. *Example 3: Reverse-Oblique Scenarios*

This example is given to illustrate the dependency of the model prediction on rupture characteristic rake angle for a $SOF = 2$ category rupture. To illustrate, the same scenario from Example 2 is used, and the only directivity parameter changed is the characteristic rake angle (90, 75, 60, 45, 30 and 15 degrees). We note that a user has the option to specify the style of faulting category, or else the category will be automatically selected based on the characteristic rake angle provided. In this example we specify $SOF = 2$ for each scenario, where the rake-based categorization would have selected $SOF = 1$ for rake angles of 15 and 30 degrees. Figure 6-10 shows the amplification predictions (T=5 sec) for these scenarios.

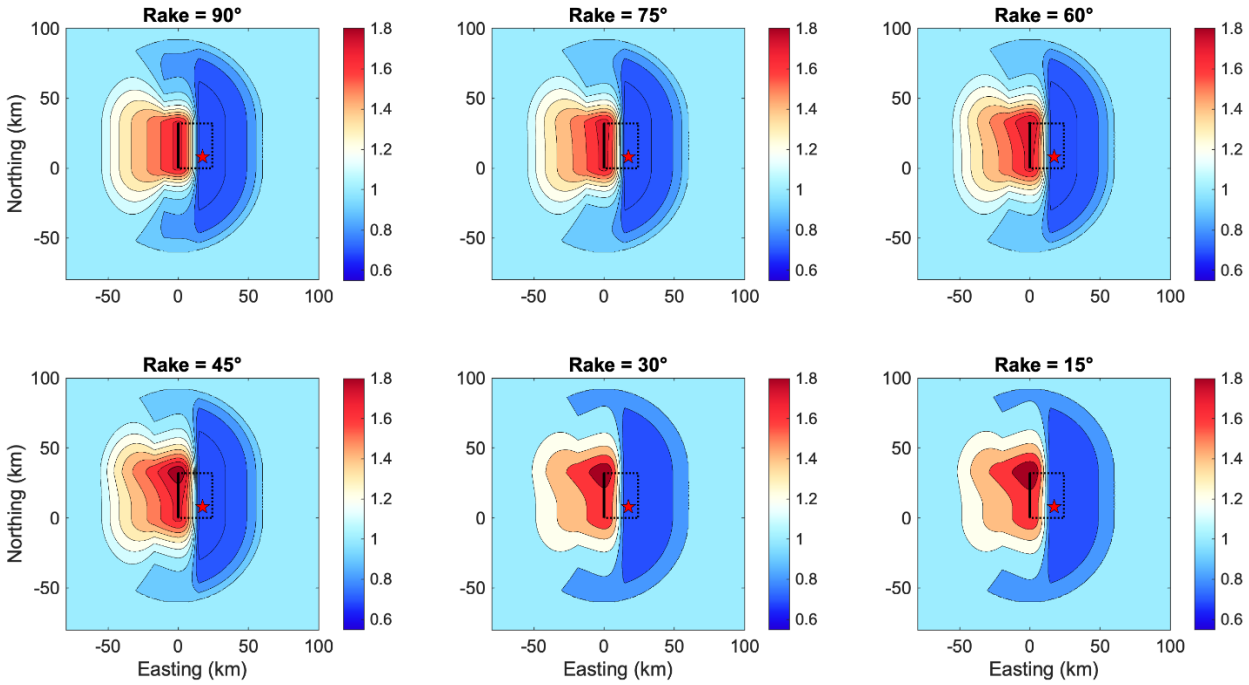

Figure 6-10. The effect of the characteristic rake angle on the predicted directivity adjustment for a $SOF = 2$ category rupture.

6.4. Example 4: Two-segment Reverse Scenario (rv7)

The previous examples all considered scenarios without any changes along strike. In this example, we use a scenario **M**7.5 reverse faulting rupture with a 45-degree bend at the midpoint. The rupture has 30-degree dip on both segments, 90-degree rake, total length of 80 km, down-dip width of 30 km, and rupture reaches the ground surface. The hypocenter is located 20 km along strike from the southern trace endpoint and at a depth of 11 km. Figure 6-11 shows the GC2 coordinates for a grid of locations surrounding the earthquake, and the model amplification at T=5 sec.

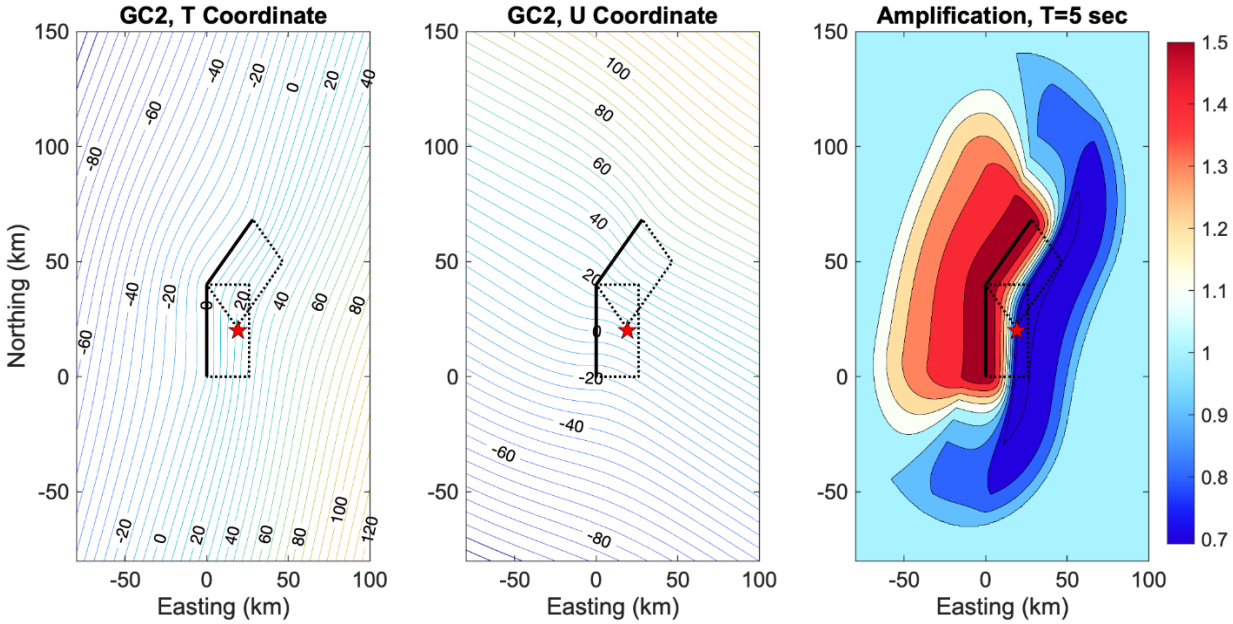

Figure 6-11. Left, Middle: GC2 for scenario rv7. Right: Model predicted T=5 sec amplification.

6.5. Example 5: 1999 Chi-Chi, Taiwan

In this example, we show the model amplification for the 1999 Chi-Chi, Taiwan earthquake using the rupture model adopted by NGA-West2. This rupture model has **M**7.62 and consists of nine strands with varying strike and dip angles as shown in Figure 6-12, with total length of 88 km and down-dip width of 37 km. The characteristic rake angle is taken as 55 degrees, and the characteristic dip is calculated as the mean dip over the 9 strands, 34 degrees. The hypocenter is located at the location shown by the star in Figure 6-12. This figure also shows the mapped model amplification at T=5 sec.

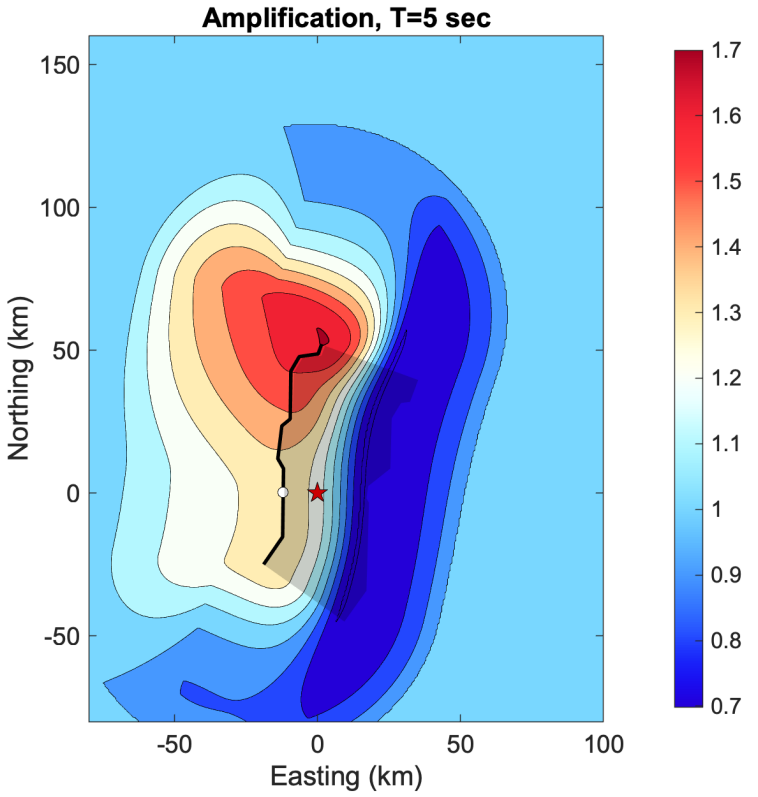

Figure 6-12. The model amplification predicted for the 1999 Chi-Chi, Taiwan earthquake at T=5 sec.

The predicted amplification from three other models is shown in Figure 6-13 (Figure 1.13 from Spudich et al., 2013). These models are described in Spudich et al. (2013); rowv4 stands for Rowshandel, sha12 stands for Shahi and Baker, and sc3b stands for Spudich & Chiou (IDP model). The general locations of forward directivity footprints approximately agree between our model, rowv4 and sc3b. The sha12 model predicts ground motion pulses and is confined near the fault trace. Both our model and sc3b predict the highest amplifications to the north of the rupture and on the footwall side of the rupture trace. The maximum amplification factors for this scenario (at T=5 sec) are approximately 1.7 (this model), 1.4 (rowv4), 1.1 (sha12), and 1.8 (sc3b). The minimum amplifications are approximately 0.7 (this model), 0.9 (rowv4), 0.9 (sha12), and 0.7 (sc3b).

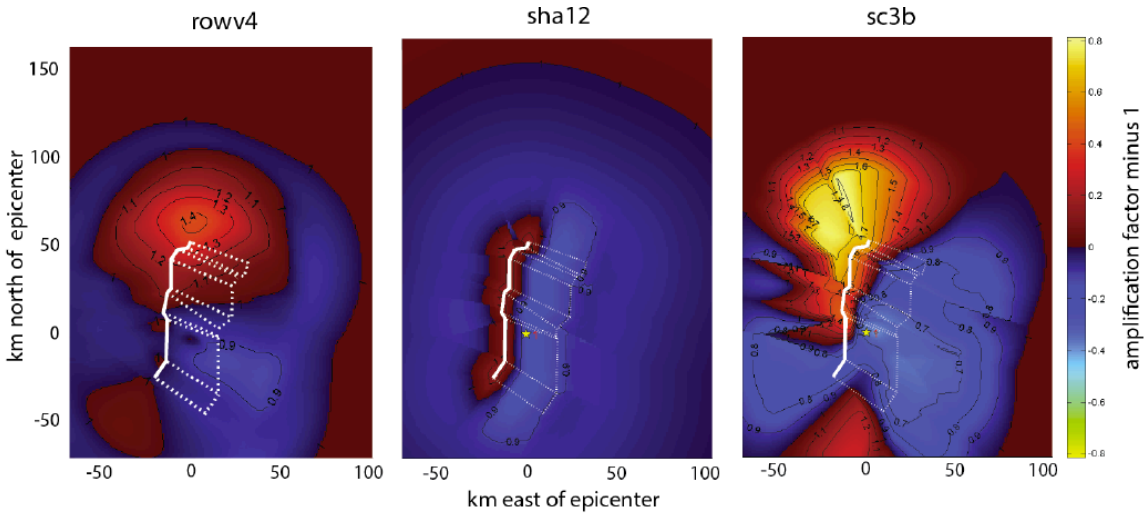

Figure 6-13. Directivity amplification predicted for the 1999 Chi-Chi, Taiwan earthquake at T=5 sec for three models: rowv4, sha12, and sc3b. Figure source: Spudich et al, (2013).

*6.6. Example 6: 1906 San Francisco, **M**7.8*

In this example, we show the model amplification for the **M**7.8 scenario earthquake representing the 1906 San Francisco event. In this case, the rupture is defined as in Aagaard et al., (2009). The rupture is 478 km in length and has a characteristic rake angle of zero degrees. Figure 6-14 shows the mapped model amplification at T=7 sec.

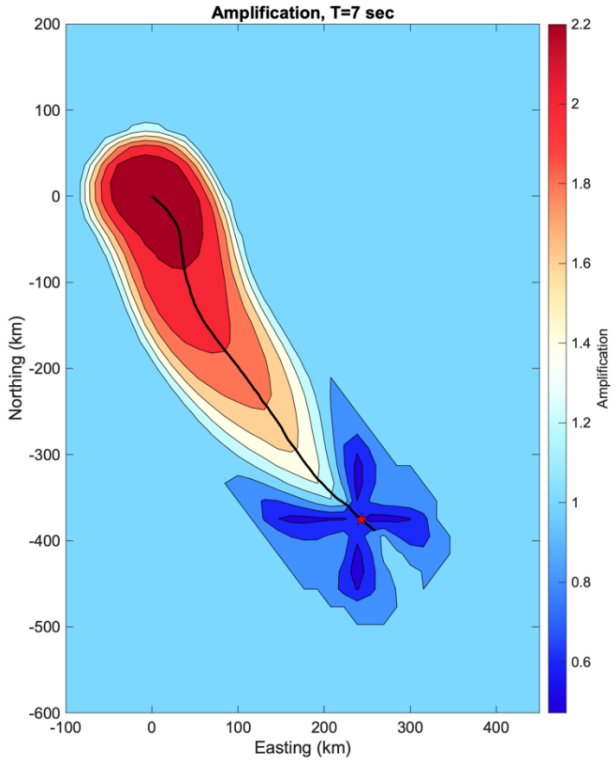

Figure 6-14. The model amplification predicted for the Aagaard et al., (2009) 1906 San Francisco earthquake, at T=7 sec.

6.7. Example 7: 2002 Denali, Alaska

In this example, we show the model amplification for the 2002 Denali, Alaska earthquake using the rupture model adopted by NGA-West2. This rupture model has **M**7.9 and is composed of three strands. Strand 1, which contains the hypocenter, is 45.1 km in length and 24 km width and is shallowly dipping (dip=32 deg) with 90-degree rake. Strand 2 is 213.7 km long and 15 km wide, with 80-degree dip and 171-degree rake. Finally, Strand 3 is 67.9 km long and 15 km wide, with 90-degree dip and 171-degree rake. To apply the model, we assume a characteristic rake of 171 degrees based on the larger rupture areas of strands 2 and 3 compared to strand 1. For the characteristic dip, we average the dip from strands 2 and 3 to arrive at 85 degrees. Figure 6-15 shows the mapped model amplification at T=5 sec.

Figure 6-16, modified from Spudich et al. (2013), shows the amplifications predicted by the model sc3b for this scenario. The regions of forward directivity generally have a similar footprint between these models, although the distance taper in sc3b reduces the effect at smaller distances than our model. sc3b also predicts much higher peak amplifications in the forward directivity zone; about 2.5 compared with 1.6 for our model. The region surrounding the hypocenter shows more pronounced differences between the models. In sc3b the region up-dip from the reverse-faulting strand (strand 1) exhibits amplification, where this region in our model is modeled as a strike-slip source (due to selecting the rupture characteristic rake angle of 171 degrees) and therefore does not model the up-dip directivity. The smallest amplification factors for the sc3b model and our model are about 0.7 and 0.53, respectively.

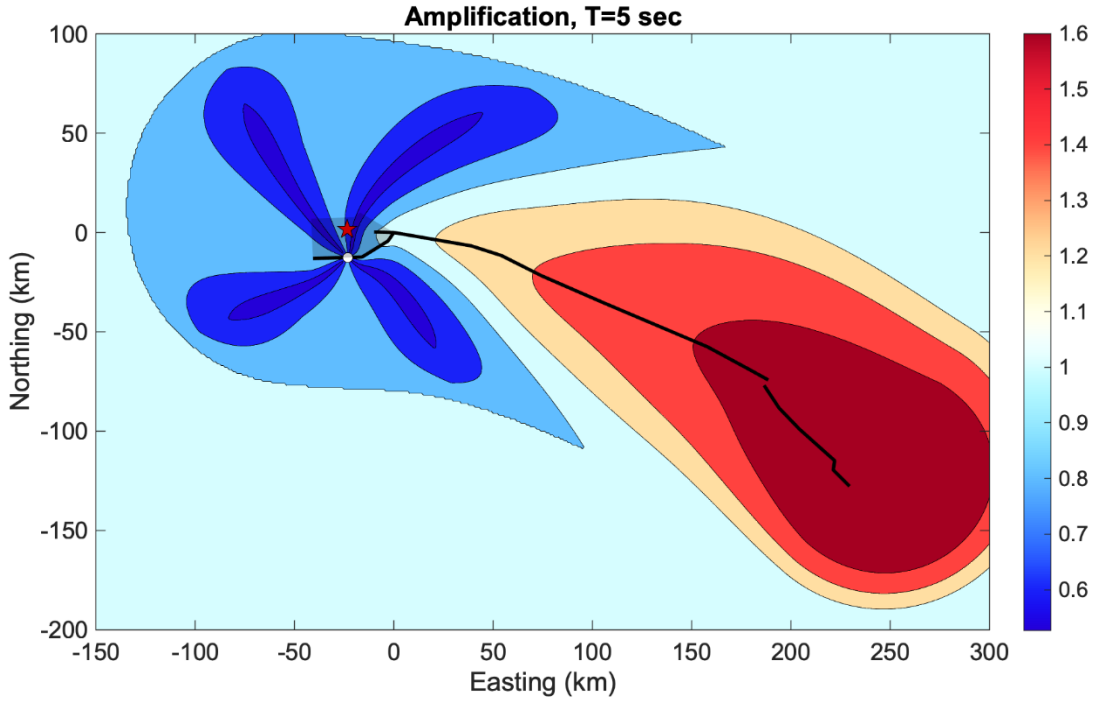

Figure 6-15. The model amplification predicted for the 2001 Denali, Alaska earthquake at T=5 sec.

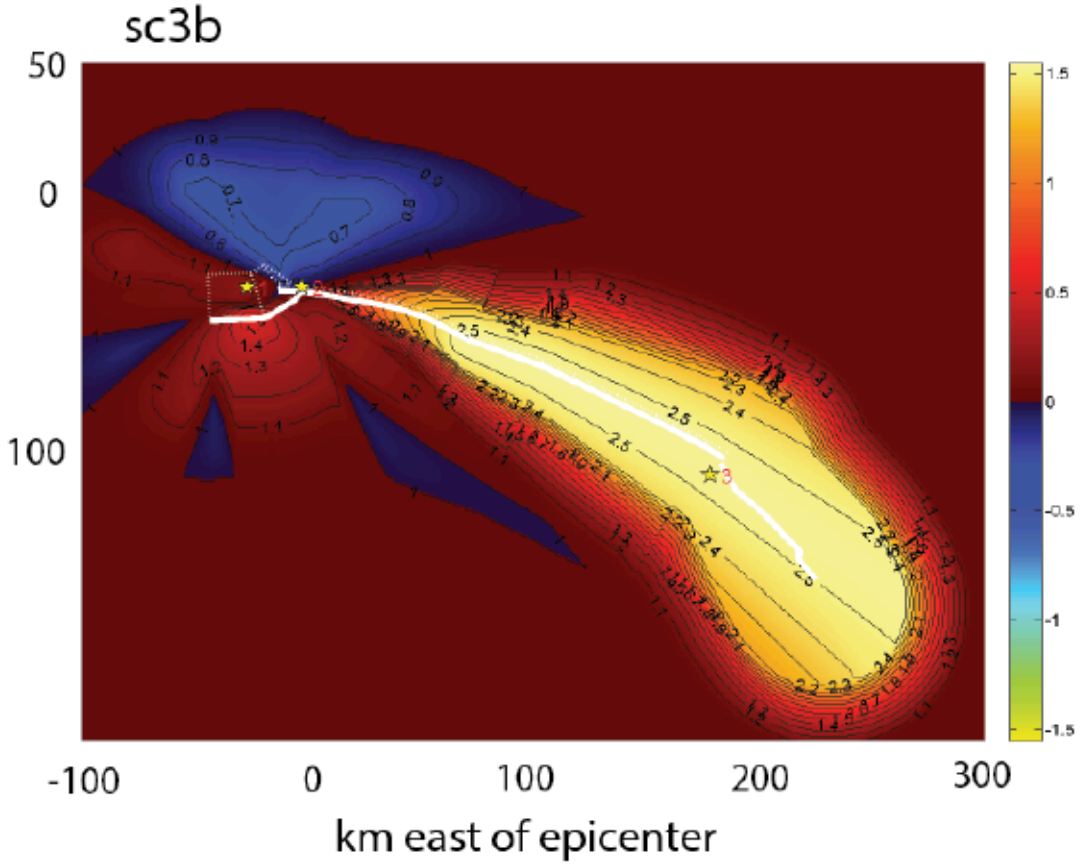

Figure 6-16. The model amplification predicted for the 2001 Denali, Alaska earthquake at T=5 sec; sc3b model. Figure source: Spudich et al, (2013). The vertical color bar at right shows (amplification-1) and the contour labels show amplification.

6.8. *Example 8: Discontinuous Rupture*

In this example, the model is applied to a hypothetical scenario earthquake. This strike-slip rupture is set up with two disconnected strands, each vertically dipping and with 22km width. The first strand has strike of 0 degrees and 40km length, with the hypocenter located 30 km from the southern end. The second has 45 degree strike and 28.28 km length. There is a gap of about 14 km between these strands, which we note is 9 km larger than the "maximum jump distance" allowed in the plausibility filters used to define UCERF3 ruptures (Field et al., 2013; Appendix T). With this example we do not suggest that this is a realistic earthquake scenario, rather we are demonstrating the flexibility of the model to accommodate ruptures with gaps between strands. Using the Leonard (2010) relationship for rupture area and magnitude, the scenario is prescribed **M**7.15. Figure 6-17 shows the components of the directivity model for this scenario, along with the predicted amplification at T=3 sec.

The application of the model to this scenario is subject to the limitations described in Section 4.5; in this case the values of directivity parameter S are artificially increased using the algorithm to convert from the coordinate U to S. This is because the S calculation includes the distance between the disconnected ruptures. The smaller the distance between segments, the weaker the artificial increase will be.

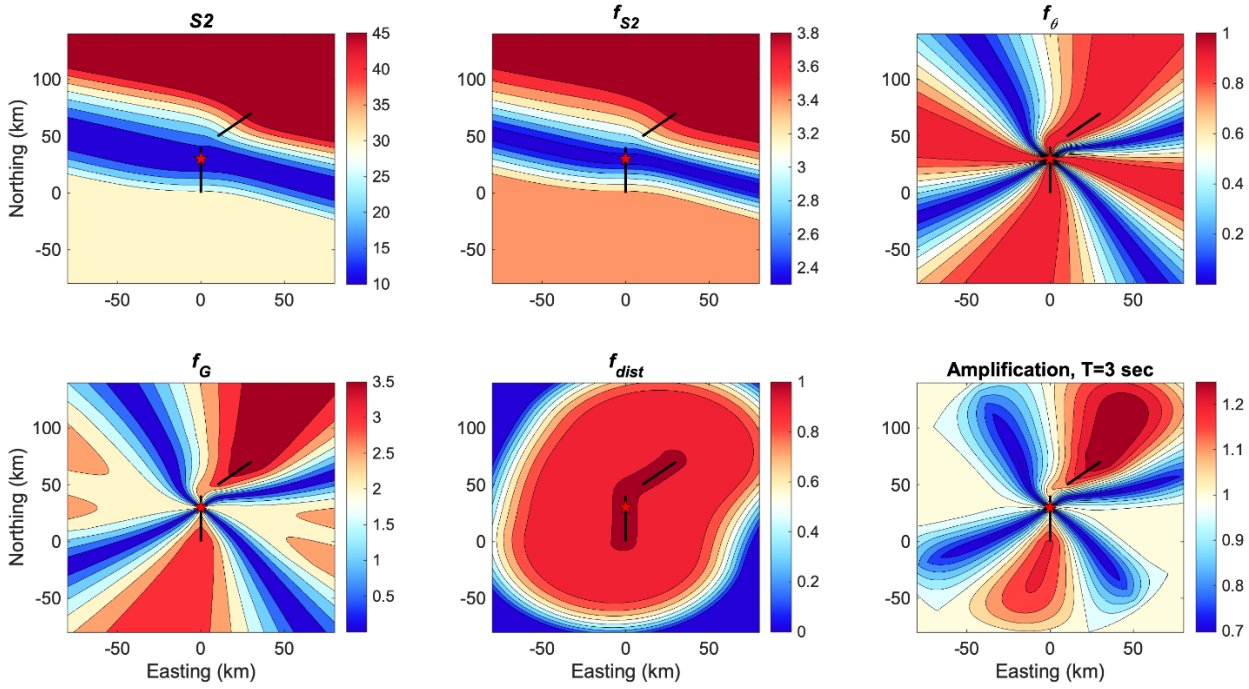

Figure 6-17. Components of the directivity model for a hypothetical discontinuous rupture scenario.

6.9. Example 9: Hypocenter Randomization

In this example, Figure 6-18 shows a map of average amplification factors for the ss3 scenario (Example 1, with 80km rupture length assuming a uniform distribution of hypocenter locations along strike). The hypocenters are placed in 1 km increments ranging from 5 to 75 km from the southern edge, and at 10 km depth.

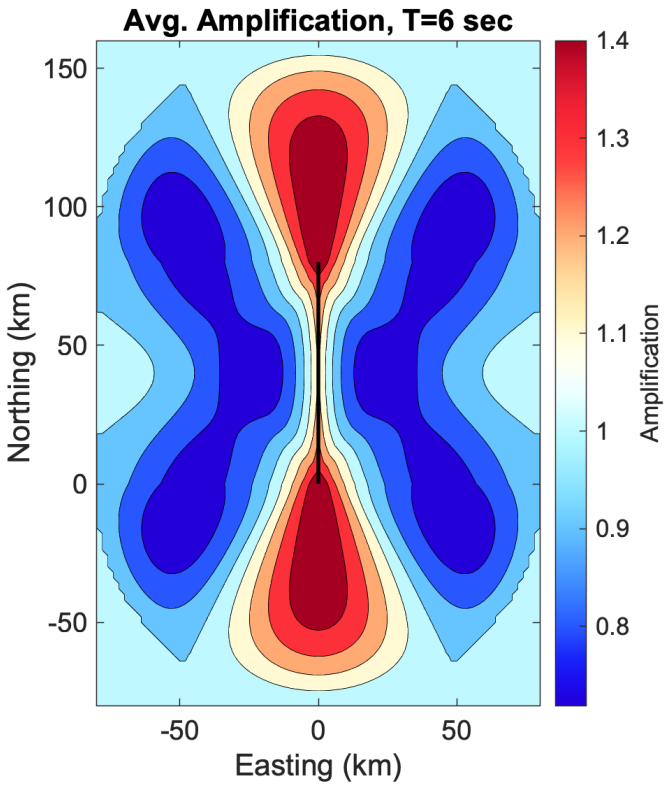

Figure 6-18. The average model amplification predicted for the ss3 scenario, with hypocenter locations assumed to vary uniformly along strike and at a fixed depth, at T=7 sec.

6.10. Example 10: Magnitude Scaling

Figure 6-19 shows amplification maps for four vertical strike-slip scenarios, each north-south striking, and with hypocenter placed at the center of the rupture plane. The maps are shown at the spectral period corresponding to the scenario peak amplification (T_{peak}). The parameters used to define these scenarios are listed in Table 6-1. Scenario 1 is **M**5.0 and has such small dimensions that the fault trace (black line) is not visible on the map. With increasing magnitude, T_{peak} and the maximum distance in the distance taper also increase.

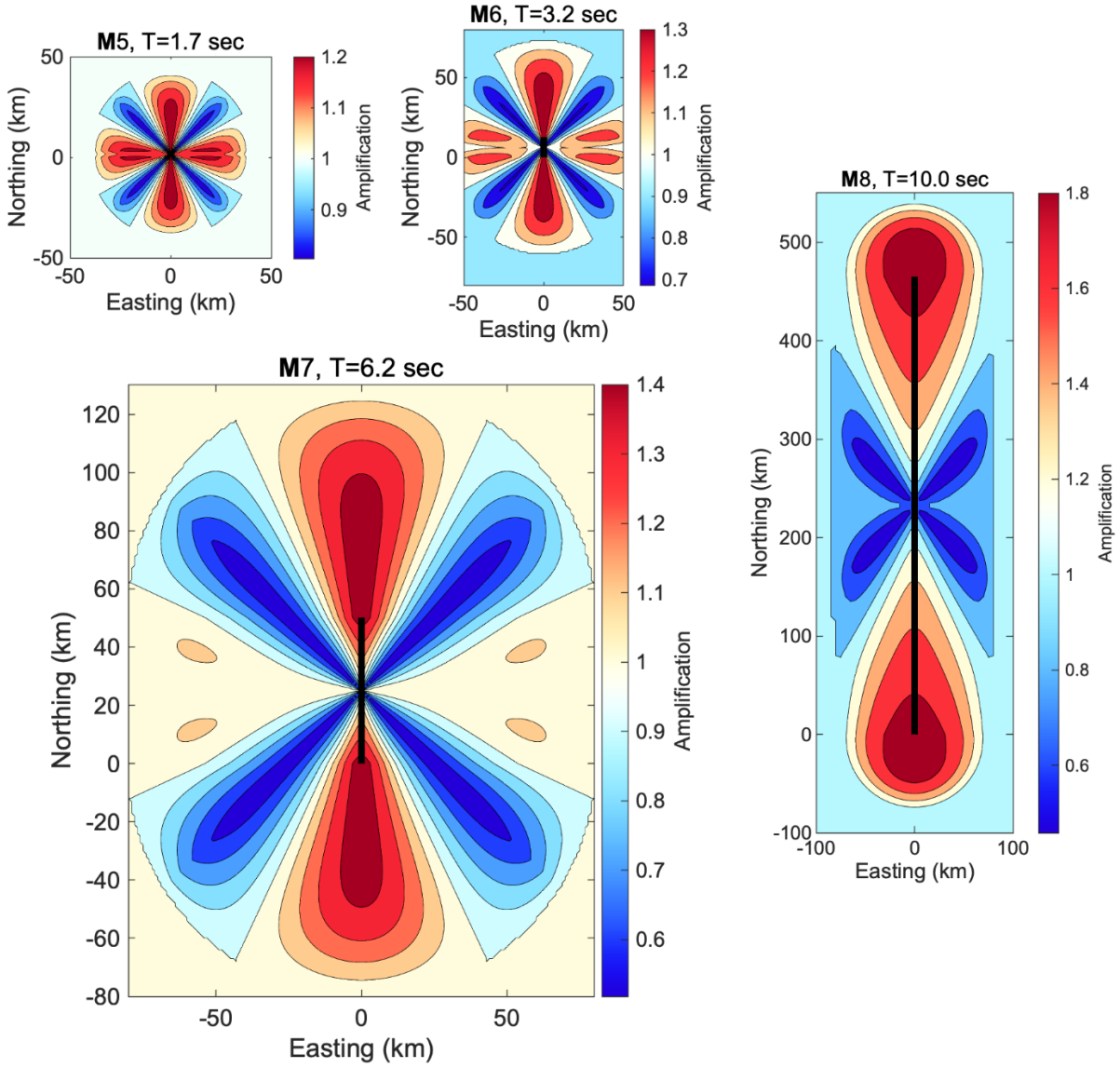

Figure 6-19. The mapped directivity adjustment (amplification) for the four strike-slip scenarios described in the text.

Table 6-1. Parameters of the scenarios used to illustrate the model behavior with magnitude.

Number	M	Length (km)	Width (km)	T_{peak} (sec)
Strike-slip 1	**5.0**	3.2	3.2	1.7
Strike-slip 2	**6.0**	12.6	8.12	3.2
Strike-slip 3	**7.0**	50.2	20.4	6.2
Strike-slip 4	**8.0**	465.0	22.0	10.0
Reverse 1	**5.0**	2.8	3.5	1.7
Reverse 2	**6.0**	11.3	8.8	3.2
Reverse 3	**7.0**	45.1	22.2	6.2
Reverse 4	**8.0**	179.5	55.7	10.0

Figure 6-20 shows amplification maps for four reverse-faulting scenarios (90-degree rake), each north-south trending, with hypocenter placed at the center of the rupture plane, and with dip of 45 degrees. The parameters used to define these scenarios are listed in Table 6-1.

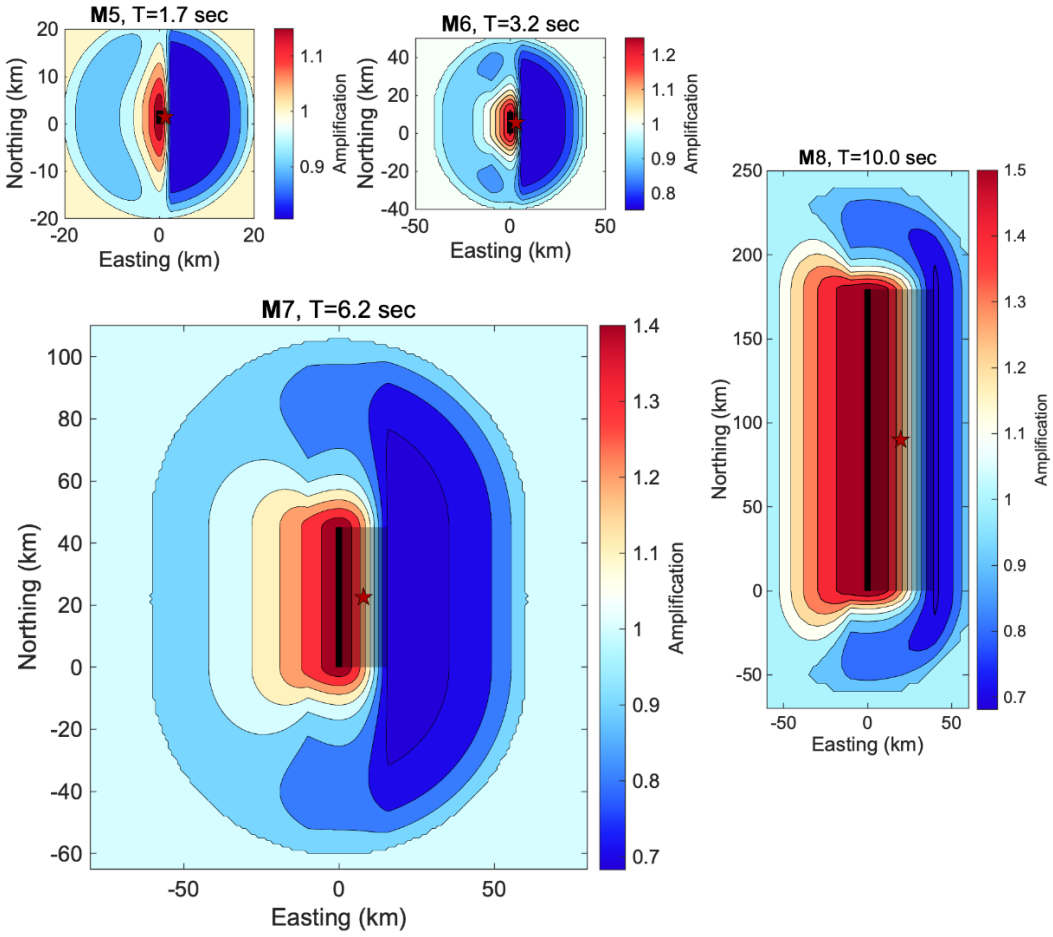

Figure 6-20. The mapped directivity adjustment (amplification) for the four reverse-faulting scenarios described in the text.

7. Conclusions

This study focuses on creating an updated directivity adjustment model. This model supersedes our BS13 and SSGA models. The model retains, for the most part, the computational simplicity of both previous versions. We value the relative computational simplicity because it allows for straightforward implementation in seismic hazard analyses. Although it is relatively simple, users will notice some degree of added model complexity. These arise from the desire to model the directivity effect as a narrowband phenomenon and to accommodate complex and multi-segment ruptures.

The current model incorporates several advances over the previous versions:

- Treatment of complex rupture geometries is handled through use of the generalized coordinate system GC2, as formulated by Spudich and Chiou (2015). With this formulation, the model boasts greatly improved flexibility compared with previous versions. The model is well-defined for any location surrounding any reasonable rupture geometry, with no known singularities.
- The model is centered because it is based on a residual analysis and therefore does not alter the GMM magnitude or distance scaling.
- The model is narrowband, meaning the peak effect scales with magnitude.
- The model is guided by finite-fault simulations with dense station arrays and strong azimuthal coverage.
- An aleatory variability adjustment model accompanies the median adjustment model.
- The level of model documentation (this report) is significantly enhanced.

With these improvements, it is our belief (and goal) that an informed user should be able to apply the model to any reasonable scenario to aid in their ground motion study.

The model is based on RotD50 within-event residual analyses and should be used to adjust existing RotD50 GMMs which do not account for directivity effects. We evaluate three NGA-W2 GMMs: Abrahamson et al. (2014), Boore et al. (2014), and Campbell and Bozorgnia (2014) and do not discern large differences between the models developed from individual GMMs versus from the average of these GMMs. Therefore, in forward application, the model is designed to be used with these models on average or individually.

The median and standard deviation adjustment models are appropriate over the period range 0.01 to 10 seconds, in the magnitude range **M**5.0-8.0, and have a footprint which is magnitude and style-of-faulting dependent, with a maximum of 80 km distance from the fault trace. The model makes several assumptions and is not without its shortcomings; the reader is referred to Section 4.5 for a discussion of these. A MATLAB implementation of the model is provided in Appendix A.

7.1. Future Work

The model itself is complete, but we would like to provide a more thorough guide for users who wish to implement it into PSHA. Specifically, in the next year we plan to:

- Provide a more complete comparison with other directivity models, including BS13 and Chiou and Youngs (2014).
- Provide instructions for using the model in PSHA. This procedure is described in Donahue et al. (2019) for other models, and we will extend it to this one.
- Provide example PSHA implementations for simple earthquake forecasts, including the Fortran language programs required for use with HAZ45, and comparisons of hazard curves for the set of examples provided in Donahue et al. (2019).
- Test the model application to UCERF3-style Ruptures. A driving force behind the current model update was the need for models which are applicable to UCERF3, e.g. Figure 7-1. We anticipate that the model is suitable for use with UCERF3, but have not yet tested it.
- Provide example PSHA implementations utilizing UCERF3, including a comparison of hazard curves with and without the directivity model.
- Potentially, prepare a directivity adjustment map database for the state of California using the catalog of UCERF3 scenarios, including hypocenter randomization. This database could be included in future PSHAs and would allow for robust directivity implementation with large savings in computation times, because the hypocenter randomization would not need to be performed.

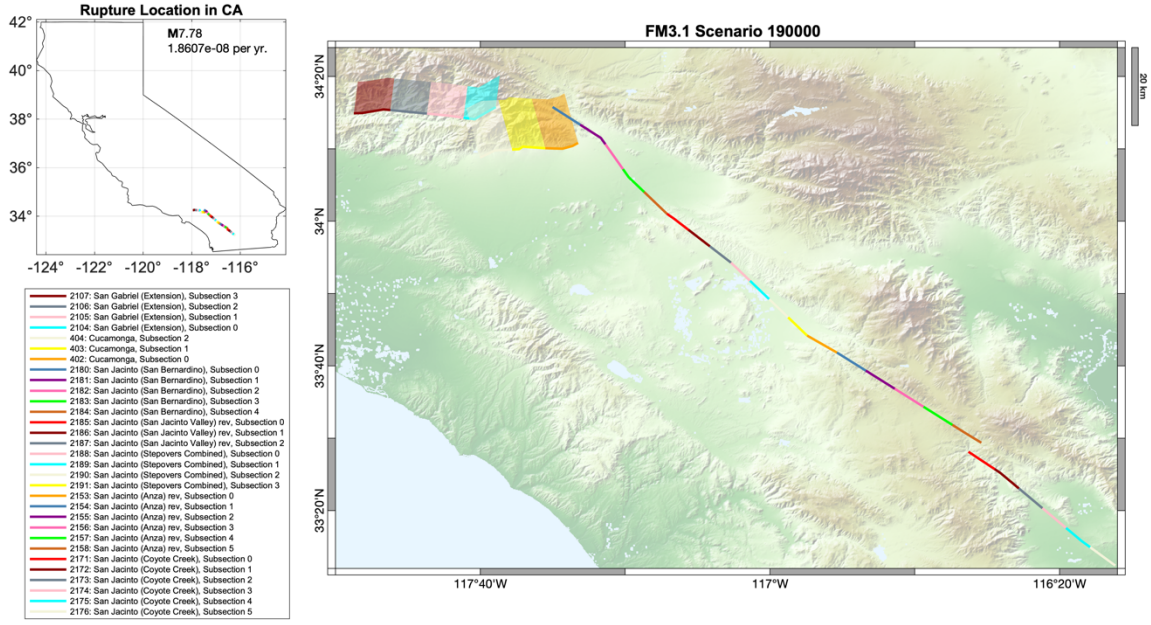

Figure 7-1. Right: A map of the UCERF3 FM3.1 earthquake scenario #190,000 (out of 253,706), which has **M**7.78, 1.8607e-8 per year rate and involves multiple segments. Top Left: The location of this scenario within California. Bottom Left: The figure legend identifying the UCERF3 named segments involved in this scenario.

8. Acknowledgements

We extend thanks to the Pacific Earthquake Engineering Research Center for making their ground motion databases, including those from NGA-West2, publicly available. Thanks to Rob Graves, Arben Pitarka, Art Frankel, Jorge Crempien, Ralph Archuleta and Fabio Silva for providing us with suites of synthetic ground motions from their (or others) simulations. We also thank Brian Chiou for providing example implementations of GC2, Linda Al Atik for several rewarding discussions, and Norm Abrahamson, Ronnie Kamai, Dave Boore, Emel Seyhan, Ken Campbell, and Yousef Bozorgnia for graciously sharing their GMM residuals. All maps in this report were created using the *READHGT* MATLAB package (Beauducel, 2020). Finally, we gratefully acknowledge the financial support for this work by the USGS under award number G18AP00092.

9. References

Aagaard, B., J.F. Hall, and T.H. Heaton (2004). Effects of Fault Dip and Slip Rake Angles on Near-Source Ground Motions: Why Rupture Directivity was Minimal in the 1999 Chi-Chi, Taiwan Earthquak., Bull. Seismol. Soc. Am., 94: 155-170.

Aagaard, B., Barall, M., Brocher, T.M., Dolenc, D., Dreger, D., Graves, R.W., Harmsen, S., Hartzell, S., Larsen, S., McCandless, K., Nilsson, S., Petersson, N.A., Rodgers, A., Sjogreen, B., and Zoback, M.L., (2009). Data files for ground motion simulations of the 1906 San Francisco earthquake and scenarios earthquakes on the northern San Andreas Fault: U.S. Geological Survey Data Series 413, 22 p. and data packages [https://pubs.usgs.gov/ds/413/]

Abrahamson, N. A. (2000). Effects of rupture directivity on probabilistic seismic hazard analysis, Proceedings from the 6th International Conference on Seismic Zonation, Palm Springs, California.

Abrahamson N.A., Walter J. Silva, and Ronnie Kamai, (2014). Summary of the ASK14 Ground Motion Relation for Active Crustal Regions. Earthquake Spectra: August 2014, Vol. 30, No. 3, pp. 1025-1055.

Aki, K. and P. Richards (1980). Quantitative Seismology, Freeman, New York.

Al Atik L, Abrahamson NA, Cotton F, Scherbaum F, Bommer JJ, Kuehn N. (2010). The variability of ground-motion prediction models and its components. Seismological Research Letters; 81(5):794-801.

Ancheta, T.D., Darragh, R.B., Stewart, J.P., Seyhan, E., Silva, W.J., Chiou, B.S.J., Wooddell, K.E., Graves, R.W., Kottke, A.R., Boore, D.M., Kishida, T., Donahue, J.L. (2013). PEER NGA-West2 Database, PEER Report 2013/03.

Bayless, J., and Somerville, P., (2013). Bayless-Somerville Directivity Model, Chapter 3 of PEER Report No. 2013/09, P. Spudich (Editor), Pacific Earthquake Engineering Research Center, Berkeley, CA.

Beauducel, F. (2020). READHGT: Import/download NASA SRTM data files (.HGT) (https://www.mathworks.com/matlabcentral/fileexchange/36379-readhgt-import-download-nasa-srtm-data-files-hgt), MATLAB Central File Exchange. Retrieved May 2, 2020.

Boore, D. M. (2010). Orientation-independent, non geometric-mean measures of seismic intensity from two horizontal components of motion, Bull. Seismol. Soc. Am. 100, 1830–1835.

Boore, D.M., J.P. Stewart, E. Seyhan, and G.M. Atkinson, (2014). NGA-West2 Equations for Predicting PGA, PGV, and 5% Damped PSA for Shallow Crustal Earthquakes. Earthquake Spectra: August 2014, Vol. 30, No. 3, pp. 1057-1085.

Bray, J. D. and A. Rodriguez-Marek (2004). Characterization of forward-directivity ground motions in the near-fault region. Soil Dynamics and Earthquake Engineering 24(11), 815–828.

Campbell, K.W., and Y. Bozorgnia (2008). NGA ground motion model for the geometric mean horizontal component of PGA, PGV, PGD and 5% damped linear elastic response spectra for periods ranging from 0.01 to 10 s, Earthq. Spectra 24, 139–172.

Campbell K.W. and Y. Bozorgnia, (2014). NGA-West2 Ground Motion Model for the Average Horizontal Components of PGA, PGV, and 5% Damped Linear Acceleration Response Spectra. Earthquake Spectra: August 2014, Vol. 30, No. 3, pp. 1087-1115.

Chiou, B. S.-J, and Spudich, P., (2013). The Chiou and Spudich Directivity Predictor DPP, in Chapter 6 of PEER Report No. 2013/09, P. Spudich (Editor), Pacific Earthquake Engineering Research Center, Berkeley, CA.

Chiou, B. S.-J., and Youngs, R. R., (2014). Update of the Chiou and Youngs NGA model for the average horizontal component of peak ground motion and response spectra, Earthquake Spectra 30, 1117–1153.

Crempien, J. G. F., and Archuleta, R. J. (2014) UCSB Method for Simulation of Broadband Ground Motion from Kinematic Earthquake Sources Seismological Research Letters, Dec 17, 2014, v. 86, p. 61-67, doi:10.1785/0220140103

Donahue, J.L, JP Stewart, N Gregor, Y Bozorgnia (2019) Ground-Motion Directivity Modeling for Seismic Hazard Applications. PEER Report 2019/03

Dreger, D., Beroza, G. C., Day, S. M., Goulet, C. A., Jordan, T. H., Spudich, P., and Stewart, J. P. (2013). Evaluation of SCEC Broadband Platform Phase 1 Ground Motion Simulation Results. Southern California Earthquake Center Report, Los Angeles, California, USA

Dreger, D. S., G. C. Beroza, S. M. Day, C. A. Goulet, T. H. Jordan, P. A. Spudich, and J. P. Stewart (2015). Validation of the SCEC Broadband Platform V14.3 Simulation Methods Using Pseudospectral Acceleration Data, Seismol. Res. Lett., 86, no. 1, doi:10.1785/0220140118.

Field, E.H., Biasi, G.P., Bird, P., Dawson, T.E., Felzer, K.R., Jackson, D.D., Johnson, K.M., Jordan, T.H., Madden, C., Michael, A.J., Milner, K.R., Page, M.T., Parsons, T., Powers, P.M., Shaw, B.E., Thatcher, W.R., Weldon, R.J., II, and Zeng, Y., (2013). Uniform California earthquake rupture forecast, version 3 (UCERF3)—The time-independent model: U.S. Geological Survey Open-File Report 2013–1165, 97 p., California Geological Survey Special Report 228, and Southern California Earthquake Center Publication 1792, http://pubs.usgs.gov/of/2013/1165/.

Frankel, A. (2009). A Constant Stress-Drop Model for Producing Broadband Synthetic Seismograms: Comparison with the Next Generation Attenuation Relations. Bull of the Seism. Soc. Am., Vol. 99, No. 2A, pp. 664-680, April 2009, doi: 10.1785/0120080079

Goulet, C.A., Abrahamson, N.A., Somerville, P.G. and K, E. Wooddell (2015). The SCEC Broadband Platform Validation Exercise: Methodology for Code Validation in the Context of Seismic-Hazard Analyses, Seismol. Res. Lett., 86, no. 1, doi: 10.1785/0220140104

Graves, R.W. and Somerville, P.G. (2006). Broadband ground motion simulations for scenario ruptures of the Puente Hills fault, 8th Nat. Conf. Earthquake Engineering, EERI, San Francisco, CA, paper no. 1052.

Graves, R.W., and Somerville, P.G. (2010). Ground Motion Simulations for Scenario Earthquakes. Presentation given at the PEER-SCEC simulations workshop, November 2011.

Graves, R.W., and A. Pitarka (2010). Broadband ground-motion simulation using a hybrid approach, Bull. Seismol. Soc. Am. 100, 2095–2123, doi: 10.1785/0120100057.

Graves, R.W., and Pitarka, A. (2014). Refinements to the Graves and Pitarka (2010) Broadband Ground-Motion Simulation Method. Seis. Res. Letters. Dec 17, 2014, 12:26. doi: 10.1785/0220140101

Leonard, M. (2010). Earthquake Fault Scaling: Self-Consistent Relating of Rupture Length, Width, Average Displacement, and Moment Release. Bull. Seism. Soc. Am., 100, 1971–1988.

Petersen, M.D., Moschetti, M.P., Powers, P.M., Mueller, C.S., Haller, K.M., Frankel, A.D., Zeng, Yuehua, Rezaeian, Sanaz, Harmsen, S.C., Boyd, O.S., Field, Ned, Chen, Rui, Rukstales, K.S., Luco, Nico, Wheeler, R.L., Williams, R.A., and Olsen, A.H., (2014), Documentation for the

2014 update of the United States national seismic hazard maps: U.S. Geological Survey Open-File Report 2014–1091, 243 p., https://dx.doi.org/10.3133/ofr20141091.

Rodriguez-Marek, A., and Cofer, W. (2009) Incorporation to Forward-Directivity into Seismic Hazard Analysis. Report prepared for Transportation Northwest. Report No. TNW2009-02, Research Agreement No. 430846

Rowshandel, B., (2006). Incorporating source rupture characteristics into ground-motion hazard analysis models, Seismol. Res. Lett. 77 , 708–722.

Rowshandel, B., (2010). Directivity correction for the Next Generation Attenuation (NGA) relations, Earthquake Spectra 26, 525–559.

Rowshandel, B., (2013). Rowshandel's NGA-West2 directivity model, Chapter 3 of PEER Report No. 2013/09, P. Spudich (Editor), Pacific Earthquake Engineering Research Center, Berkeley, CA.

Rowshandel, B., (2018). Capturing and PSHA Implementation of Spatial Variability of Near-Source Ground Motion Hazard, Conference on Geotechnical Earthquake Engineering and Soil Dynamics V, June 10–13, 2018, Austin, Texas

Shahi, S. K., (2013). A Probabilistic Framework to Include the Effects of Near-Fault Directivity in Seismic Hazard Assessment, Ph.D. Thesis, Stanford University, Stanford, CA, 226 pp.

Shahi, S. K., and Baker, J. W., (2013). Shahi-Baker Directivity Model, Chapter 4 of PEER Report No. 2013/09, P. Spudich (Editor), Pacific Earthquake Engineering Research Center, Berkeley, CA.

Somerville, P.G., N. Smith, R. Graves and N. Abrahamson (1997). Modification of empirical strong ground motion attenuation relations for the amplitude and duration effects of rupture directivity. *Seismol. Res. Lett*. 68, 199-222.

Somerville, P.G. (2003). Magnitude scaling of the near fault rupture directivity pulse. Physics of the Earth and Planetary Interiors 137, 201-212.

Spagnulo, E., Herrero, A., and Cultrera, G. (2012). The effect of directivity in a PSHA framework. Geophysical Journal International 191, 616-626.

Spudich, P., and Chiou, B. S-J., (2006). Directivity in preliminary NGA residuals, Final Project Report for PEER Lifelines Program Task 1M01, available at http://quake.usgs.gov/~spudich/pdfs_for_web_page/Spudich&Chiou1M01_FinalReport-v6.pdf, 49 pp.

Spudich, P., and Chiou, B. S.-J., (2008). Directivity in NGA earthquake ground motions: Analysis using isochrone theory, Earthquake Spectra 24, 279–298.

Spudich, P., and Chiou, B. S.-J., (2013). The Spudich and Chiou NGA-West2 directivity model, Chapter 5 of PEER Report No. 2013/09, P. Spudich (Editor), Pacific Earthquake Engineering Research Center, Berkeley, CA.

Spudich, P., and Chiou, B. S.-J., (2015). Strike-Parallel and Strike-Normal Coordinate System Around Geometrically Complicated Rupture Traces- Use by NGA-West2 and Further Improvements. US Geological Survey Open File Report 2015-1028, 28p.

Spudich, P., Bayless, J. R., Baker, J. W., Chiou, B. S.-J., Rowshandel, B., Shahi, S. K., and Somerville, P. G., (2013). Final Report of the NGA-West2 Directivity Working Group, Pacific Earthquake Engineering Research Center Report PEER-2013/09, Berkeley, CA, 130 pp.

Spudich, P., Chiou, B. S-J., Graves, R., Collins, N., and Somerville, P. G., (2004). A formulation of directivity for earthquake sources using isochrone theory, U.S. Geological Survey Open File Report 2004-1268.

Spudich, P., Rowshandel, B., Shahi, S.K., Baker, J.W. and Chiou, B. S-J. (2014). Comparison of NGA-West2 Directivity Models. Earthquake Spectra Aug 2014, Vol. 30, No. 3 pp. 1199-1221

Stewart, J., Bozorgnia, Y., Bray, J., Donahue, J., Graves, R., Idriss, I.M., Luco, N., Mahin, S., and Shantz., T. (2016). PEER Directivity End-Users Panel. Presentation given at the 2016 COSMOS Annual Meeting and Technical Session, 18 Novermber 2016.

Tarbali, K., Bradley, B., and Baker, J. W. (2016). Seismic hazard analysis and ground motion selection considering directivity effects. Poster presentation at the 2016 QuakeCore Annual Meeting.

Tothong, P., Cornell, C.A., Baker, J.W., (2007), Explicit Directivity-Pulse Inclusion in Probabilistic Seismic Hazard Analysis, Earthquake Spectra, Volume 23, No. 4, pages 867-891, Earthquake Engineering Research Institute.

10. Bibliography

No publications have resulted from this research as of this date

11. Project Data

Our research uses publicly available data from the Pacific Earthquake Engineering Research Center (https://peer.berkeley.edu). The RotD50 database of simulations utilized in this project is provided, with permission from the authors, in Appendix C.

Appendix A: MATLAB Functions

This appendix contains a hyperlink to download the following MATLAB files:

- Bea20_Example.m: a script which calculates the directivity effect for an example scenario and produces a map, making use of the functions below.
- GC2.m: Calculates the GC2 coordinates. This function is a conversion to MATLAB of Brian Chiou's R functions (pers. comm.)
- Bea20.m: a function which implements the directivity model

Please follow this link to download:

https://drive.google.com/drive/folders/1ceWVe7Zm-SDFQXSAGjo7aPopDjZ5Vc7F?usp=sharing

Appendix B: Graphical Interpretation of ϕ

In the following figures, the cross-section view of a generic dipping fault is shown, where the rupture plane is the thick black line and the point of interest on the ground surface is given by the black inverted triangle. The GC2 T ordinates are with respect to the origin, po. The dip angle of the rupture is δ and we solve for ϕ for three site location cases. The angle ϕ is independent of the hypocenter location.

Case 1: $T < 0$; on the footwall side.

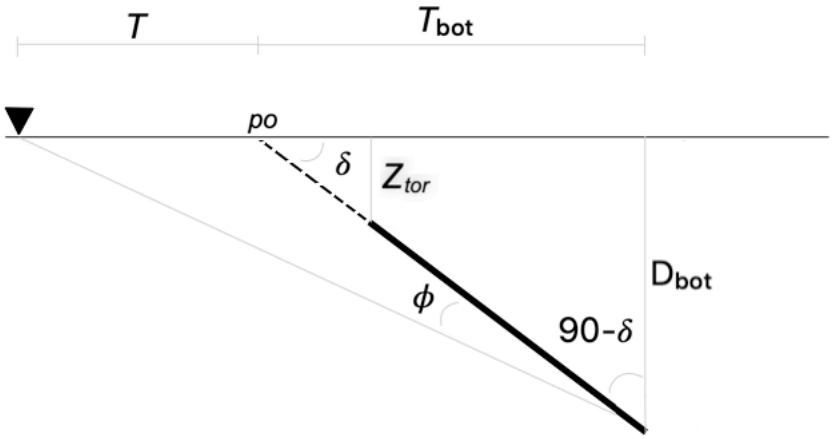

Here we can see that:

$$\tan(\phi + 90 - \delta) = \frac{|T| + T_{bot}}{D_{bot}}$$

Noting that the absolute value of T is taken because T is negative on the footwall side of the fault, and solving for ϕ:

$$\phi = \delta - 90 + \tan^{-1}\frac{|T| + T_{bot}}{D_{bot}}$$

Case 2: $0 \leq T \leq T_{bot}$; on the hanging wall but between the origin and T_{bot}.

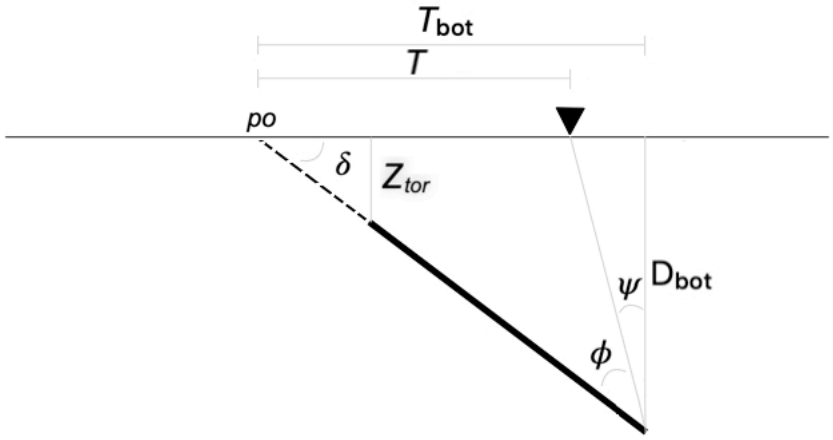

Here we can see that:

$$\psi = \tan^{-1}\frac{T_{bot}-T}{D_{bot}}$$

$$90 - \delta = \psi + \phi$$

and solving for ϕ:

$$\phi = 90 - \delta + \tan^{-1}\frac{T_{bot}-T}{D_{bot}}$$

Case 3: $T > T_{bot}$; on the hanging wall, beyond the rupture plane surface projection.

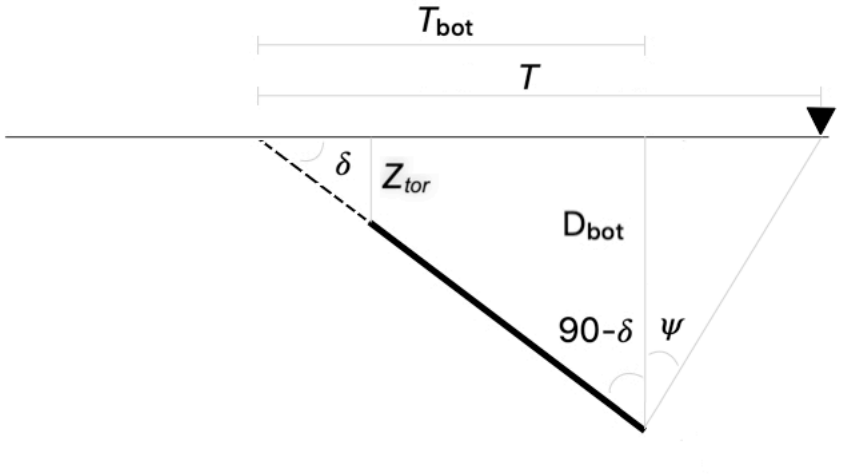

Here we can see that:

$$\psi = \tan^{-1}\frac{T - T_{bot}}{D_{bot}}$$

$$\phi = 90 - \delta + \psi$$

Therefore:

$$\phi = 90 - \delta + \tan^{-1}\frac{T - T_{bot}}{D_{bot}}$$

Appendix C: Directivity in Simulations

Table C-1 lists the simulation scenarios used in the analysis, and a brief description of each is provided below. This appendix contains two parts, part one is the full set of results described in Section 5.1 (residual maps and figures showing trends of residuals with the directivity predictors). Part two is a suite of RotD50 "flatfiles" for each simulation set. Both parts can be downloaded from this URL:

https://drive.google.com/drive/folders/1ceWVe7Zm-SDFQXSAGjo7aPopDjZ5Vc7F?usp=sharing

Sets 1-2, 4, 9-11: SCEC Broadband Platform (BBP) simulations calculated using Graves and Pitarka (2014) and Crempien and Archuleta (2014) of varying scenario earthquake. The simulations selected include two strike slip scenarios (**M**6.2 and 6.6) and two reverse faulting scenarios (**M**5.5 and 6.6). Each scenarios includes 30 simulations stations on each of two half-rings with rupture distances of 20 and 50 km. Additionally, these scenarios include up to 50 different realizations of the kinematic source model, including random hypocenter locations. With all of these different combinations, the azimuthal coverage is very dense. These simulations all use theoretical 1D (plane-layered) Green's functions and are performed for a reference site condition (no Vs30 scaling).

Set 3: Low frequency (f<5 Hz) simulations of a generic **M**6.45 strike-slip earthquake, calculated by Rob Graves using a 3D finite difference approach. The dense grid of near-source simulation stations surrounds the rupture.

Sets 5-6: SCEC Broadband Platform (BBP) simulations of the 1992 Landers earthquake, calculated using Graves and Pitarka (2014) and Crempien and Archuleta (2014). These simulations use theoretical 1D (plane-layered) Green's functions, and results are available for multiple realizations of the kinematic source model.

Set 7: Broadband simulations of a generic **M**7.5 strike-slip earthquake, calculated and verified against the NGA-West1 GMMs by Frankel (2009). This simulation uses a hybrid methodology with the stochastic method at high frequencies, and has stations with full azimuthal coverage.

Set 8: Broadband simulations of the **M**7.8 1906 San Francisco earthquake (Aagaard et al., 2009) calculated by Rob Graves. These simulations use a hybrid method consisting of a 3D finite element method at low frequencies and a stochastic method at high frequencies. This is the largest magnitude simulation considered.

Set 12: Broadband simulations of a **M**7.2 Puente Hills blind thrust fault scenario, calculated by Graves and Somerville (2006, 2010). These simulations incorporate heterogeneous fault rupture and effects of complex geology in LA basin region. This is the largest reverse faulting simulation used.

Table C-1. Simulations used in the model development.

Set #	Simulation Method Name	Event/Scenario Name	Additional References	Simulation Method Detail	M	1D/3D Velocity model	Highest Usable Freq (Hz)	Style of Faulting
1	Graves & Pitarka (2014)	Generic strike-slip with stations at 20, 50 km	Dreger et al., (2013, 2015); Goulet et al., (2015)	Hybrid, Broadband	6.2	1D	10	Strike-Slip
2	Crempien and Archuleta (2014)	Generic strike-slip with stations at 20, 50 km	Dreger et al., (2013, 2015); Goulet et al., (2015)	Broadband Deterministic, theoretical GFs	6.2	1D	10	Strike-Slip
3	Graves and Pitarka v2016	Generic strike-slip	Graves and Pitarka (2014)	Finite Difference, Low Freq	6.45	3D	5	Strike-slip
4	Graves & Pitarka (2014)	Generic strike-slip with stations at 20, 50 km	Dreger et al., (2013, 2015); Goulet et al., (2015)	Hybrid, Broadband	6.6	1D	100	Strike-Slip
5	Crempien and Archuleta (2014)	Landers 1992	Dreger et al., (2013, 2015); Goulet et al., (2015)	Broadband Deterministic, theoretical GFs	7.22	1D	10	Strike-Slip
6	Graves & Pitarka (2014)	Landers 1992	Dreger et al., (2013, 2015); Goulet et al., (2015)	Hybrid, Broadband	7.22	1D	100	Strike-Slip
7	Frankel (2009)	Generic Strike-Slip	~	Hybrid, Broadband	7.5	1D	20	Strike-Slip

Set #	Simulation Method Name	Event/Scenario Name	Additional References	Simulation Method Detail	M	1D/3D Velocity model	Highest Usable Freq (Hz)	Style of Faulting
8	Graves (2009)	San Francisco 1906	Aagaard et al., (2009)	Hybrid: Staggered-Grid Finite Element, Stochastic for f >1 Hz	7.8	Both (3D low F, 1D high F)	10	Strike-Slip
9	Graves & Pitarka (2014)	Generic reverse with stations at 20, 50 km	Dreger et al., (2013, 2015); Goulet et al., (2015)	Hybrid, Broadband	5.5	1D	10	Reverse
10	Graves & Pitarka (2014)	Generic reverse with stations at 20, 50 km	Dreger et al., (2013, 2015); Goulet et al., (2015)	Hybrid, Broadband	6.6	1D	10	Reverse
11	Crempien and Archuleta (2014)	Generic reverse with stations at 20, 50 km	Dreger et al., (2013, 2015); Goulet et al., (2015)	Broadband Deterministic, theoretical GFs	5.5	1D	10	Reverse
12	Graves and Pitarka (2010)	Puente Hills blind thrust	Graves and Somerville (2006; 2010)	Hybrid; 3D Finite Difference for F<1, 1D Stochastic for F>1	7.2	Both (3D low F, 1D high F)	10	Reverse

Appendix D: Directivity in NGA-W2 Data

This appendix contains the full set of results described in Section 5.2, including residual maps and figures showing trends of residuals with the directivity predictors. These can be downloaded from this URL:

https://drive.google.com/drive/folders/1ceWVe7Zm-SDFQXSAGjo7aPopDjZ5Vc7F?usp=sharing